Research Square

Preprints are preliminary reports that have not undergone peer review.
They should not be considered conclusive, used to inform clinical practice,
or referenced by the media as validated information.

Probabilistic Calibration of a Closed-loop Cardiac Electromechanical Model with Application to Cardiac Resynchronization Therapy

Ester Bergantin
University of Trento
Federica Caforio
University of Graz
Francisco Sahli Costabal
Pontificia Universidad Católica de Chile
Christoph M. Augustin
Medical University of Graz
Simone Pezzuto
simone.pezzuto@unitn.it

University of Trento

Article

Keywords: Patient-specific modeling, Electrophysiology, Cardiac resynchronization therapy, Ven-tricular dyssynchrony, Eikonal model, Bayesian optimization, Uncertainty quantification

Posted Date: April 16th, 2026

DOI: https://doi.org/10.21203/rs.3.rs-9303831/v1

License: This work is licensed under a Creative Commons Attribution 4.0 International License.
Read Full License

Additional Declarations: No competing interests reported.

Version of Record: A version of this preprint was published at npj Digital Medicine on August 27th, 2026.
See the published version at https://doi.org/10.1038/s41746-026-03149-5.

Probabilistic Calibration of a Closed-loop Cardiac Electromechanical Model with Application to Cardiac Resynchronization Therapy

Ester Bergantin[1], Federica Caforio[2,3,4], Francisco Sahli Costabal[5,6,7], Christoph M. Augustin[3,4], and Simone Pezzuto*[1,8]

[1]Laboratory of Mathematics for Biology and Medicine, Department of Mathematics, University of Trento, Italy
[2]Department of Mathematics and Scientific Computing, NAWI Graz, University of Graz, Austria
[3]Gottfried Schatz Research Center, Division of Medical Physics and Biophysics, Medical University of Graz, Austria
[4]BioTechMed-Graz, Austria
[5]Department of Mechanical and Metallurgical Engineering, School of Engineering, Pontificia Universidad Católica de Chile, Chile
[6]Institute for Biological and Medical Engineering, Schools of Engineering, Medicine and Biological Sciences, Pontificia Universidad Católica de Chile, Chile
[7]Millennium Institute for Intelligent Healthcare Engineering, iHEALTH, Chile
[8]Euler Institute, Università della Svizzera italiana, Switzerland

Abstract

Cardiac conduction disorders such as left bundle branch block (LBBB) induce ventricular dyssynchrony and increase the risk of heart failure. Cardiac resynchronization therapy (CRT) improves cardiac function in approximately 70 % of patients; however, optimizing patient selection and pacing strategy remains challenging. We present a patient-specific computational framework that integrates physics-based modeling with Bayesian personalization to simulate cardiac electromechanical function and acute response to CRT. Patient-specific anatomies are reconstructed from cardiac MRI, and electrical activation is modeled using a three-dimensional Eikonal formulation with probabilistic inference of the Purkinje network from ECG data via Bayesian Optimization. This approach enables uncertainty quantification by identifying multiple activation patterns consistent with clinical observations. Electrical activation is coupled to a closed-loop cardiovascular model (CircAdapt), calibrated using Constrained Bayesian Optimization to match MRI-derived volumetric measurements. The framework enables the simulation of multiple pacing strategies and the non-invasive estimation of their acute hemodynamic effects, while propagating electrophysiological uncertainty to mechanical outputs. Relying exclusively on non-invasive data and maintaining low computational cost, the proposed framework provides a scalable approach toward uncertainty-aware cardiac digital twins for personalized CRT planning.

Keywords: Patient-specific modeling; Electrophysiology; Cardiac resynchronization therapy; Ventricular dyssynchrony; Eikonal model; Bayesian optimization; Uncertainty quantification.

1 Introduction

In the heart, synchronous electrical activation of the ventricles is a necessary condition for optimal cardiac pump function [1, 2]. When this physiological activation is disrupted by conduction disorders such as left bundle branch block (LBBB) [3], the risk of developing heart failure increases significantly [4].

Cardiac resynchronization therapy (CRT) has been shown to be an effective treatment for patients with heart failure (NYHA class II–IV) with reduced ejection fraction (<35 %) and ventricular conduction delay (QRS complex >120 ms) [5]. In clinical practice, this primarily applies to patients with LBBB. In this therapy, electrical activation and mechanical contraction are resynchronized by electrical stimulation of both ventricles. Various pacing protocols have been proposed and tested to optimize response to CRT, ranging from conventional biventricular pacing (the current gold standard) to novel strategies such as conduction system pacing (CSP) [6].

*Corresponding author. E-mail: simone.pezzuto@unitn.it

Clinical CRT trials have shown a positive response in approximately 70 % of patients, corresponding to an improvement in pump function [7]. This implies that a substantial proportion of patients may either receive suboptimal therapy or undergo unnecessary device implantation. Inadequate response can be related to suboptimal left ventricular (LV) lead positioning or the presence of regional myocardial scarring [8]. In this context, a tailored approach is desirable, as multiple patient-specific factors contribute to the design of the optimal therapeutic strategy. Moreover, these factors are derived from multimodal sources, such as electrocardiography, cardiac imaging, and echocardiography, making their integration into the clinical decision-making process challenging.

Computational models of the heart have reached a level of maturity that enables their use as integrative tools for combining multimodal clinical data and for exploring therapeutic scenarios in a mechanistically interpretable manner [9]. This paradigm has been extensively investigated over the past decade [10, 11, 12], leading to the concept of the cardiac digital twin [13]. However, despite several promising applications [14, 15], clinical translation remains limited. Major challenges include the high computational cost of cardiovascular models required for post-CRT electromechanical and hemodynamic assessment [16], the limited identifiability of model parameters from non-invasive clinical data [17], and the presence of both epistemic and aleatoric uncertainties, which must be quantified to enable reliable clinical decision-making [18]. In particular, current approaches either lack detailed personalization of the cardiac conduction system or do not explicitly account for uncertainty in model predictions, limiting their reliability for patient-specific decision support. This gap motivates the development of computational frameworks that combine detailed electrophysiological personalization with uncertainty-aware prediction of hemodynamic response.

In this work, we address these challenges by introducing an efficient cardiovascular modeling framework, building on previous electromechanical approaches [19], combined with a Bayesian pipeline for parameter calibration and uncertainty quantification across model components [20]. The forward model integrates two main components: an electrophysiology (EP) module and a lumped, closed-loop cardiovascular model (CircAdapt) [21, 22]. The EP component is based on the anisotropic Eikonal equation for the three-dimensional myocardium [23, 24], coupled to a parametrized Purkinje network to account for both orthodromic and antidromic activation [20, 25]. Using a lead-field formulation within a patient-specific torso model [26], the framework enables the simulation of physiological ECG signals that can be directly compared with clinical recordings. The cardiovascular component is driven by region-averaged activation times via the MultiPatch approach [27], enabling the simulation of regional myocardial strain, pressure–volume loops, and global hemodynamic response at a prescribed heart rate. Importantly, the overall framework remains computationally efficient while retaining physiological fidelity [28].

A distinctive feature of this framework is the explicit personalization of the Purkinje network from ECG data, enabling a patient-specific reconstruction of ventricular activation patterns [20, 29]. Specifically, we adopt a Bayesian Optimization (BO) framework and Approximate Bayesian Computation (ABC) [20] to infer a posterior distribution of Purkinje network configurations consistent with the observed ECG. In this work, we extend this probabilistic personalization to the cardiovascular component in two ways. First, uncertainty in the electrophysiological model (encoded in the posterior distribution of Purkinje networks) is propagated to the mechanical and hemodynamic outputs. Second, we calibrate a subset of identifiable cardiovascular parameters using patient-specific measurements derived from Cardiac Magnetic Resonance (CMR), namely left and right atrial and ventricular volumes at end-diastole and end-systole. A key methodological component is the adoption of a constrained Bayesian optimization (CBO) approach [30]. While individual parameter values may be physiologically admissible, their combination can lead to non-physiological model states. The constrained formulation addresses this issue by learning the feasible region of the parameter space during the optimization process, thereby ensuring physiologically consistent solutions [31, 18]. Overall, the proposed framework enables calibration to patient-specific data while explicitly accounting for uncertainty in both electrophysiological and hemodynamic predictions.

This capability is particularly relevant for the patient-specific evaluation of CRT strategies [32, 33, 15]. First, the electrophysiological (EP) personalization enables an accurate reconstruction of the baseline activation pattern prior to device implantation. Second, the framework allows the simulation of multiple pacing scenarios, enabling the assessment of the acute cardiovascular response and the non-invasive estimation of post-CRT hemodynamic metrics in a statistically robust manner. In this work, we evaluate the proposed framework in a cohort of heart failure patients with heterogeneous characteristics, including the presence of myocardial scar, who underwent CRT following a diagnosis of conduction disturbances [34]. For each patient, the model is anatomically personalized using cardiac imaging data and calibrated to reproduce both the baseline ECG and observed volumetric measurements. Subsequently, several pacing

strategies are explored, ranging from conventional left ventricular epicardial pacing to conduction system pacing (CSP), the latter enabled by the explicit representation of the Purkinje network within the model. Finally, the framework allows the assessment of how uncertainty in electrical activation (arising from variability in Purkinje network geometry) affects predicted hemodynamic outcomes, providing insight into the robustness of patient-specific simulations.

A schematic representation of the workflow is shown in Figure 1, highlighting the integration of electrophysiological personalization, uncertainty quantification, and hemodynamic modeling within the proposed framework.

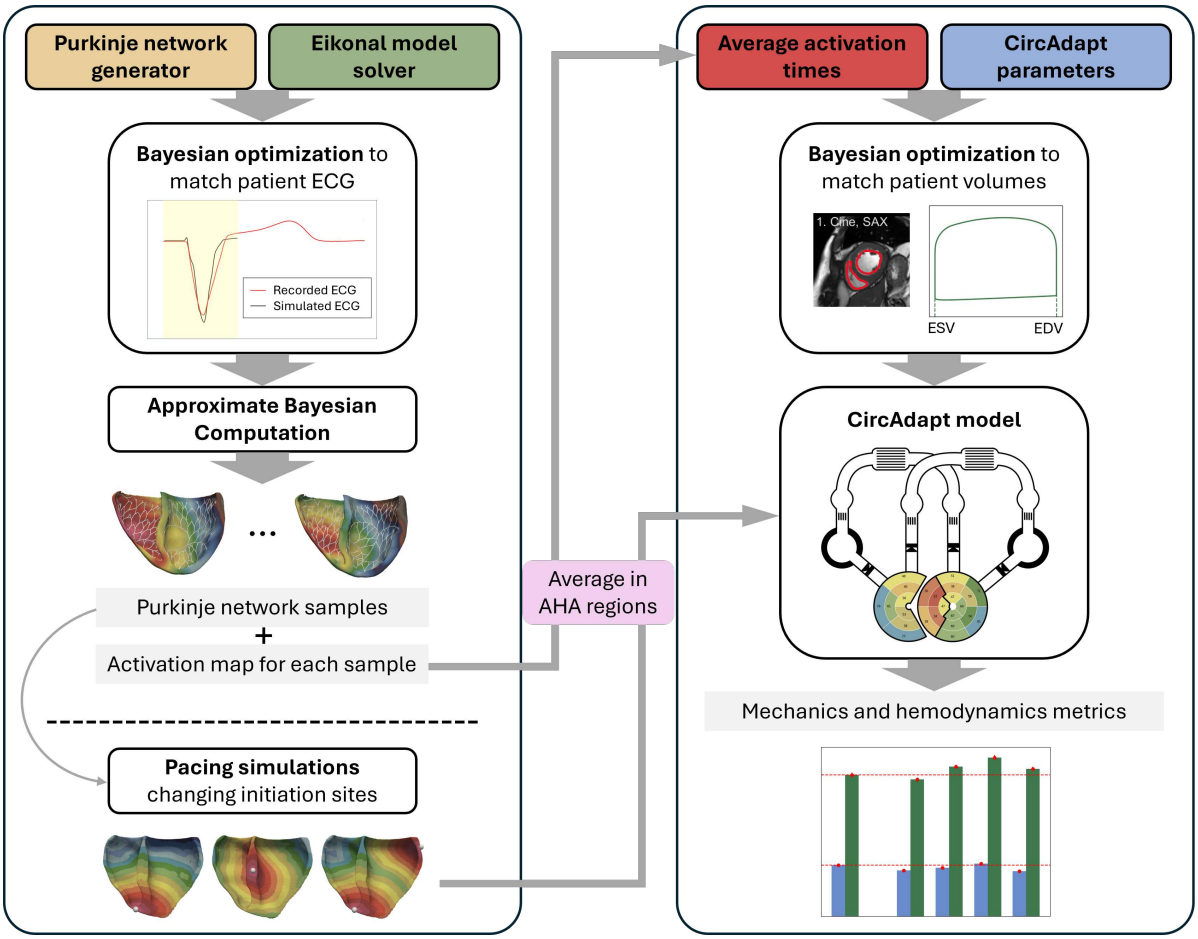

Figure 1: Schematic representation of the modeling workflow. Purkinje network geometry and electrophysiological (EP) parameters are identified using a probabilistic approach (BO+ABC) to reproduce the patient-specific LBBB ECG. Activation maps are computed with the Eikonal model and used to simulate different pacing strategies. Region-averaged activation times (AHA segmentation) are provided as input to CircAdapt to compute mechanical and hemodynamic metrics, while model parameters are calibrated independently using constrained Bayesian optimization (CBO) to match CMR-derived volumes.

2 Results

This section presents the application of the proposed uncertainty-aware framework to four patients with LBBB. The numerical validation of the electrophysiological (EP) personalization pipeline, including the recovery of ground-truth parameter distributions from synthetic ECG data, has been previously reported in [20]. Here, we demonstrate the complete pipeline on a representative LBBB case study, with a focus on its integration with the mechanical and hemodynamic components (Section 2.1).

We then assess the robustness of the CircAdapt calibration procedure through a synthetic recovery test and evaluate parameter identifiability (Sections 2.2 and 2.3). Finally, we investigate the predicted acute response to different pacing strategies across the patient cohort, reporting both electrophysiological and mechano-hemodynamic outcomes (Section 2.4).

Uncertainty in model predictions, arising from the probabilistic identification of Purkinje network configurations, is quantified and propagated throughout all analyses.

2.1 End-to-end pipeline: representative LBBB case study

To simulate the mechanical and hemodynamic outcomes of LBBB and CRT, we first model the electrical activation in the ventricles of patients with LBBB (see Section 4.1 for methodological details). Starting from the $N_{\text{sample}} = 30$ Purkinje networks obtained from probabilistic EP personalization via BO and ABC (Section 4.4.2), each network is coupled to the myocardium, and the Eikonal-based forward model is used to compute three-dimensional ventricular activation maps and corresponding ECGs (Figure 2a–b). Figure 2a shows the activation map for one representative network, while Figure 2b reports five ECG leads across all 30 simulations.

The activation maps exhibit a pattern consistent with LBBB, characterized by early septal activation and delayed activation of the left ventricular free wall (LVfw). The simulated ECGs show quantitative variability across different Purkinje network configurations, while preserving consistent waveform morphology, indicating that the posterior distribution captures the characteristic LBBB pattern.

Activation maps are then averaged over AHA regions (Figure 2c) and used as input to the CircAdapt model (Sections 4.2 and 4.3). The resulting pressure–volume (PV) loops for both ventricles (Figure 2d) are nearly indistinguishable across all samples, indicating that variability in the EP model has a negligible impact on global mechanical and hemodynamic outputs.

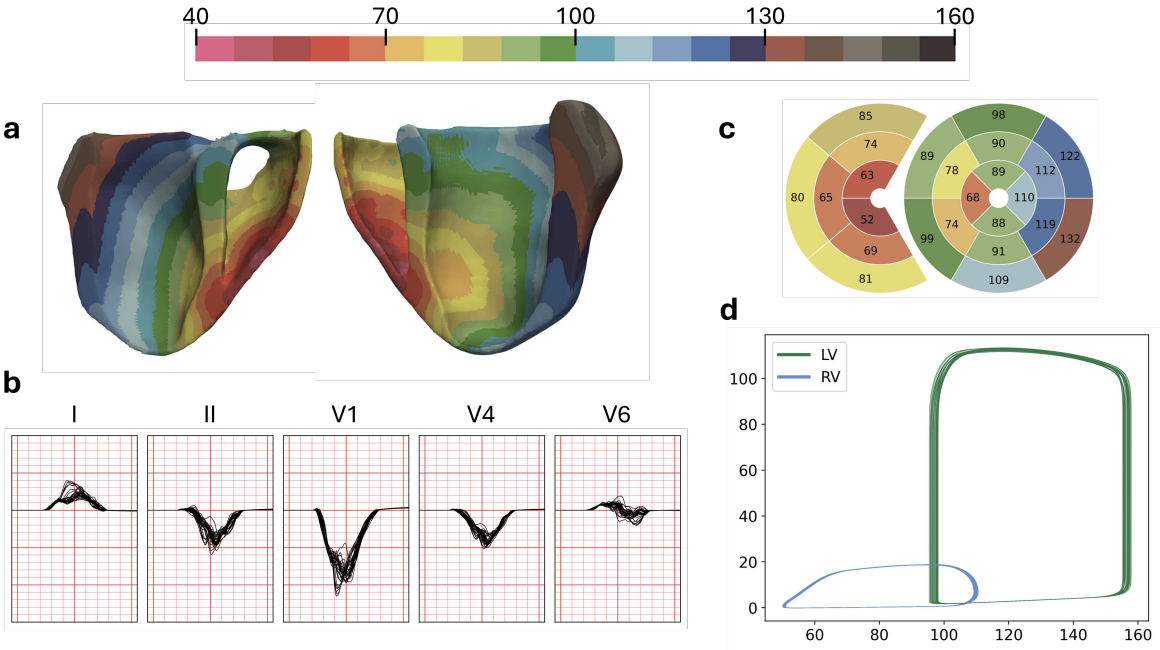

Figure 2: Main steps of the forward modeling pipeline for a representative LBBB patient. **a**: Three-dimensional ventricular activation map for one representative Purkinje network. **b**: Simulated ECGs (five leads shown) across 30 Purkinje network realizations. **c**: AHA bullseye map of region-averaged activation times for one representative simulation. **d**: Pressure–volume (PV) loops of the left and right ventricles across the 30 CircAdapt simulations.

All simulations were performed on a workstation equipped with an AMD Ryzen Threadripper 3990X (64-core, 2.9 GHz) processor, 128 GB of RAM, and an NVIDIA GeForce GT 710 GPU. Purkinje network generation, the Eikonal solver, and CircAdapt simulations were executed on a single CPU core, except for the Eikonal problem, which was solved on GPU using a CUDA-based implementation [26].

Table 1 reports the average computational time per simulation (mean ± standard deviation over N_{sample} samples). The reported times include: (i) Purkinje network generation for a fixed number of 20 branch generations (see [20] for details), (ii) solution of the coupled Purkinje–myocardium Eikonal problem, and (iii) convergence of the CircAdapt model. Convergence is defined as a relative difference below 0.1 % between pressure–volume loops of consecutive beats. ECG computation and regional averaging of activation times are negligible (<1 s). CircAdapt requires approximately 0.40 s of wall-clock time per

simulated second, exceeding real-time performance. The low computational cost per simulation makes the pipeline suitable for iterative personalization.

	LV tree [s]	RV tree [s]	Coupling [s]	CircAdapt [s]
Patient 1	7.28 ± 0.86	4.37 ± 1.49	28.95 ± 3.90	13.13 ± 0.95
Patient 2	7.53 ± 1.17	4.62 ± 0.17	49.15 ± 5.72	8.42 ± 4.76
Patient 3	12.03 ± 0.78	8.50 ± 1.67	47.88 ± 8.82	7.38 ± 4.16
Patient 4	4.29 ± 1.90	3.76 ± 1.68	38.38 ± 6.53	6.81 ± 3.73

Table 1: Average computational time per simulation (mean ± standard deviation, in seconds) over 30 samples for each patient, broken down by pipeline component. Additional steps (ECG computation and regional averaging) require less than 1 s and are not included.

2.2 Calibration robustness: synthetic recovery test

The robustness of the calibration procedure is evaluated through a synthetic recovery test in a representative patient. We consider the subset of identifiable parameters for Patient 2 (see Sections 2.3 and 4.4.5), using the baseline values reported in Table 6 as ground truth. In this test, the electrophysiological model is kept fixed, and only the cardiovascular (CircAdapt) parameters are calibrated to match volumetric measurements.

Model outputs generated from these parameters are corrupted with multiplicative Gaussian noise, with a noise level corresponding to 5 % relative variability (see Section 4.4.5), and used as target values in the CBO algorithm. Figure 3 reports the mean and standard deviation of the relative error for each parameter across 20 simulations with independent noise realizations.

The reported parameters correspond to key vascular and myocardial properties of the CircAdapt model, including reference pressures, flow, and contractility (see Table 6 for detailed definitions).

The recovered parameters show mean relative errors between 5.5 % and 9.7 %. Given that calibration is performed using noisy volumetric targets only, these errors are consistent with the limited information content of the observations and support practical recovery of the identifiable parameter subset. This interpretation is further examined through the identifiability analysis based on the reduced sensitivity matrix and Fisher Information Matrix in the following section.

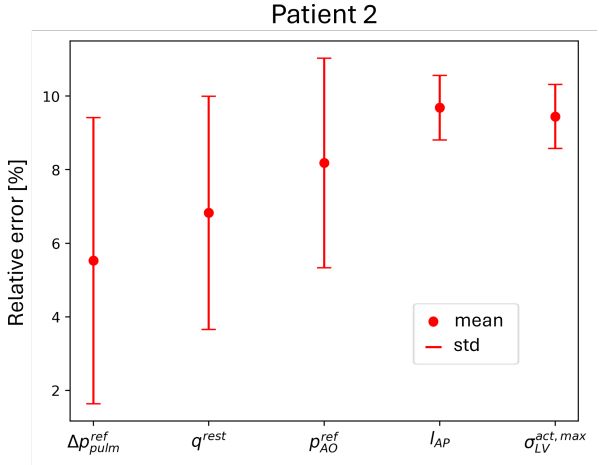

Figure 3: Mean and standard deviation of the relative error for each parameter across 20 simulations with independent noise realizations, obtained from the synthetic recovery test on Patient 2. Parameter definitions are reported in Table 6.

2.3 CircAdapt: identifiability and calibration

For the calibration of the CircAdapt model, a variance-based global sensitivity analysis (GSA) [35] was first performed separately for each patient. In the GSA, a subset of parameters was fixed to patient-specific values (e.g., wall volumes and cardiac cycle length derived from clinical data), while the remaining

parameters were varied around their baseline physiological values (Table 6). The N_{sa} most influential parameters were selected by retaining those with a total Sobol index greater than 0.1.

Parameter identifiability within this subset was then assessed via QR decomposition with column pivoting of the normalized sensitivity matrix S, evaluated at the baseline parameter vector. This yielded a reduced set of N_p locally identifiable parameters. Calibration was subsequently performed using constrained Bayesian optimization (CBO) in this reduced parameter space, while the remaining parameters were fixed at their baseline values. At the calibrated optimum, identifiability was reassessed by computing the condition number $k = s_{\max}/s_{\min}$ of the reduced sensitivity matrix S_{red}, together with the Fisher Information Matrix (FIM) [36]. Full methodological details are provided in Section 4.4.

Table 2 summarizes, for each patient, the parameter selection and identifiability analysis. Open triangles indicate parameters selected by the global sensitivity analysis, while filled triangles denote the identifiable subset retained after QR decomposition. The last two columns report the condition number of the reduced sensitivity matrix S_{red} at baseline (k_{bas}) and at the calibrated optimum (k_{opt}); a condition number below 10^3 is taken as indicative of practical local identifiability [37].

	$\sigma_{\mathrm{LV}}^{\mathrm{act,max}}$	Δt_{AV}	$p_{\mathrm{AO}}^{\mathrm{ref}}$	$p_{\mathrm{AP}}^{\mathrm{ref}}$	k_{AP}	l_{AO}	l_{AP}	l_{VP}	$\Delta p_{\mathrm{sys}}^{\mathrm{ref}}$	$\Delta p_{\mathrm{pulm}}^{\mathrm{ref}}$	q^{rest}	k_{bas}	k_{opt}
Patient 1	▲		▲	△		△	▲	△	△	▲	▲	66	254
Patient 2	▲		▲	△		△	▲		△	▲	▲	102	366
Patient 3	▲					▲	▲	△	▲	▲	△	82	75
Patient 4	△	▲	▲		▲	△	△		△	▲	▲	14	95

Table 2: Parameter selection and identifiability across patients. Open triangles (△) denote parameters selected by the global sensitivity analysis, and filled triangles (▲) denote parameters retained in the identifiable subset after QR decomposition. The last two columns report the condition number of the reduced sensitivity matrix at baseline (k_{bas}) and at the calibrated optimum (k_{opt}).

The normalized FIMs at the calibrated optimum for all patients are shown in Fig. 4. The diagonal entries reflect parameter sensitivities, while off-diagonal terms quantify parameter correlations. The FIM patterns are consistent with the condition numbers reported in Table 2, which remain below the identifiability threshold for all patients. Although a moderate increase in the condition number is observed at the optimum, the reduced sensitivity matrices remain well-conditioned, indicating that calibration does not lead to loss of practical identifiability.

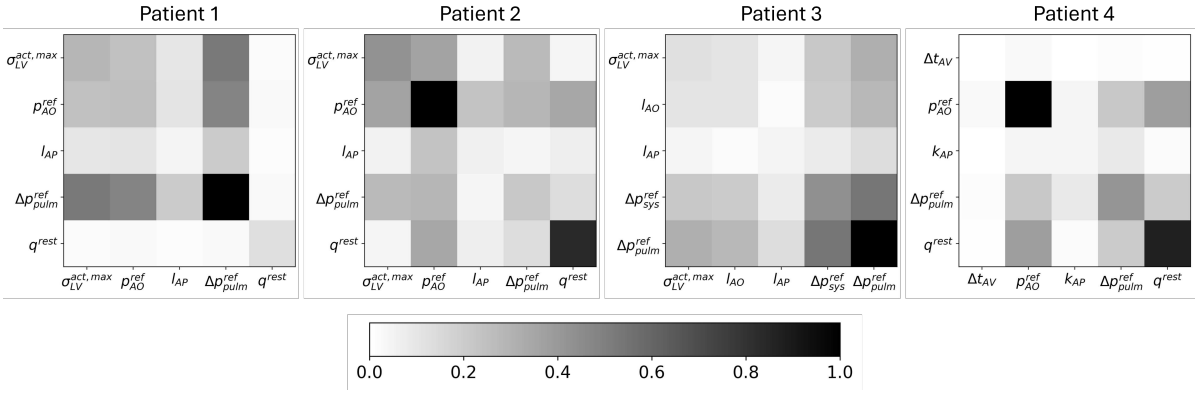

Figure 4: Normalized Fisher Information Matrices (FIM) for the four patients, evaluated at the calibrated optimal parameter values. Diagonal entries represent parameter sensitivities, while off-diagonal terms indicate correlations between identifiable parameters.

A comparison between the parameter ranking at baseline and at the calibrated optimum reveals changes in relative sensitivities, reflecting the nonlinear and coupled nature of the model. Some parameters become less informative after calibration, while others gain influence. The FIM also indicates moderate correlations between certain parameters; however, these remain limited and do not compromise identifiability of the selected parameter subset.

Following this analysis, the model was calibrated independently for each patient using the CBO algorithm. Regional activation times from a single representative posterior EP sample were used as

input to the mechanical model. Calibration accuracy was assessed by computing the relative error between simulated and CMR-derived volumes (LV and RV end-diastolic and end-systolic volumes, and LA and RA end-diastolic volumes).

To evaluate robustness with respect to electrophysiological uncertainty, the calibration errors were computed across all 30 posterior samples. Table 3 reports the mean and standard deviation of the relative errors for each output and patient. The results show overall good agreement between simulated and target volumes. The limited variability across samples further confirms that uncertainty in the EP model has negligible impact on mechanical and hemodynamic outputs, consistent with the findings from the forward simulations.

	$\varepsilon_{\text{rel}}^{\text{LV,ED}}$ [%]	$\varepsilon_{\text{rel}}^{\text{LV,ES}}$ [%]	$\varepsilon_{\text{rel}}^{\text{RV,ED}}$ [%]	$\varepsilon_{\text{rel}}^{\text{RV,ES}}$ [%]	$\varepsilon_{\text{rel}}^{\text{LA,ED}}$ [%]	$\varepsilon_{\text{rel}}^{\text{RA,ED}}$ [%]
Patient 1	15	25	13	17 ± 1	15 ± 1	3 ± 1
Patient 2	1	8	5	9	12	12
Patient 3	20 ± 1	18 ± 1	24	21 ± 1	30 ± 1	24
Patient 4	8 ± 1	22 ± 1	4	8	15	1

Table 3: Relative errors between simulated and CMR-derived cavity volumes. LV: left ventricle; RV: right ventricle; LA: left atrium; RA: right atrium; ED: end-diastole; ES: end-systole. Errors are reported as mean ± standard deviation over the N_{sample} posterior samples, reflecting variability due to electrophysiological uncertainty.

2.4 Acute response to CRT: simulation outcomes

For pacing simulations, different initiation sites were set for each pacing protocol, using the N_{sample} Purkinje networks obtained from the EP optimization. Section 4.5.2 describes the different pacing sites in the myocardium, while the evaluation metrics are described in Section 4.5.4.

2.4.1 Electrophysiological outcomes

Figure 5 shows the average activation times across AHA regions for LBBB and the different pacing strategies in a representative patient (Patient 1). Values are reported as mean and standard deviation over the $N_{\text{sample}} = 30$ posterior samples.

As expected, LBBB exhibits delayed activation of the left ventricular free wall (LVfw). RV apical pacing (RVAP) produces a heterogeneous apex-to-base activation pattern in both ventricles, with persistent delay in the LVfw. LV septal pacing (LVSP) reduces LVfw activation times but induces early activation of the interventricular septum (IVS). Standard biventricular pacing without delay (BiVP-1) results in early LVfw activation but maintains an apex-to-base gradient in the RV. Introducing delays in one lead (BiVP-2 and BiVP-3) improves either RV homogeneity or LV activation timing, but not both. In contrast, BiVP-4, with delays applied to both leads, achieves more homogeneous and synchronous activation.

Among all strategies, left bundle branch pacing (LBBP) produces the most synchronous activation pattern, improving both intra- and inter-ventricular coordination and further reducing activation times compared to BiVP-4.

The variability across samples is generally low, except for LBBB, LBBP, and BiVP-4, where larger dispersion is observed, particularly in the LVfw. This variability is not physiological but arises from reduced identifiability of left ventricular conduction parameters when activation is primarily driven by the right ventricle. In such cases, the contribution of the left Purkinje network to the ECG is limited, allowing multiple parameter configurations to fit the data. This leads to a broader posterior distribution of Purkinje networks and increased variability in activation maps.

Consistent trends are observed across patients (Figure 6). Patients 1, 3 and 4 exhibit similar patterns in activation timing and variability, with LBBP achieving the most synchronous activation. In contrast, Patient 2 shows a reduced response to pacing, with only modest improvements in activation times and no clear gain in synchrony with LBBP. This behavior is likely related to extensive myocardial scar, modeled as non-viable tissue (i.e., an conduction obstacle), which influences the overall EP activation pattern. As previously reported, scar tissue can disrupt the relationship between electrical and mechanical activation, even when located away from late-activated regions [38].

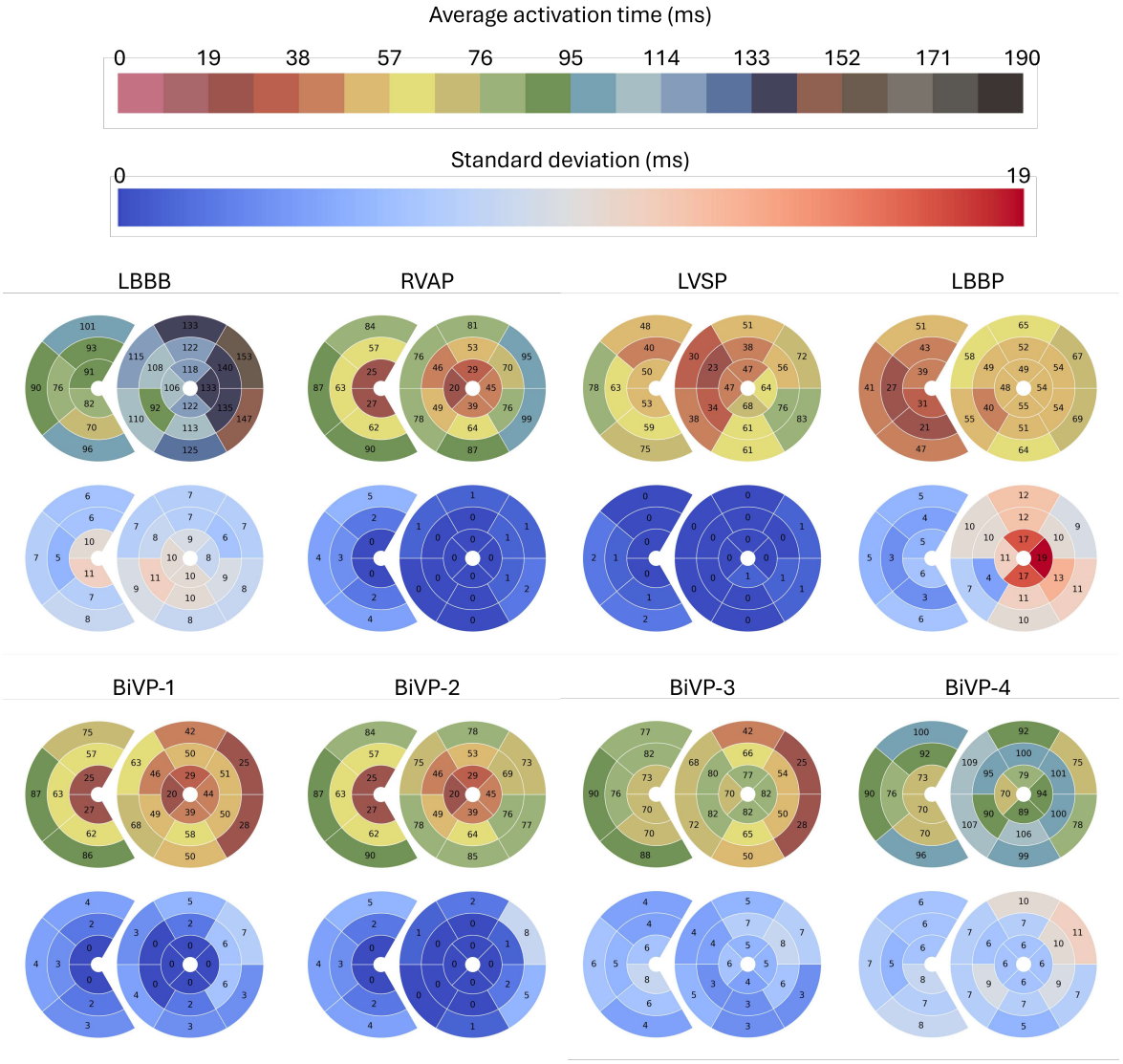

Figure 5: Activation maps for each pacing strategy in bullseye representation, showing mean activation times across N_{sample} samples and corresponding standard deviation.

Table 4 summarizes the electrophysiological metrics defined in Section 4.5.4 for each pacing strategy, averaged over the N_{sample} samples. The LBBB configuration serves as the pathological reference. To compare pacing strategies, metrics are evaluated jointly: for each metric, the best values are highlighted (see Section 4.5.4), and a score ("mark") is assigned by counting the number of optimal entries. Overall, LBBP and BiVP-4 consistently achieve the highest scores across patients, indicating superior electrical resynchronization.

2.4.2 Mechanical and hemodynamic outcomes

Table 5 reports, for each patient, the absolute values of the mechanical and hemodynamic metrics defined in Section 4.5.4 at the pathological LBBB baseline, together with the mean relative percentage variation computed over the 30 posterior samples with respect to the baseline. For each metric, the pacing strategy yielding the most favorable outcome is highlighted.

Overall, the hemodynamic response to pacing is heterogeneous across both patients and metrics. No single pacing configuration consistently outperforms the others in all cases, underscoring the patient-specific nature of the acute response to CRT. All percentage variations are computed on a per-patient basis and are therefore intended to support intra-patient comparisons across pacing strategies, rather than absolute comparisons between subjects.

Figure 7 reports the maximum rate of pressure rise ($\max \mathrm{d}P/\mathrm{d}t$) in the left and right ventricles for

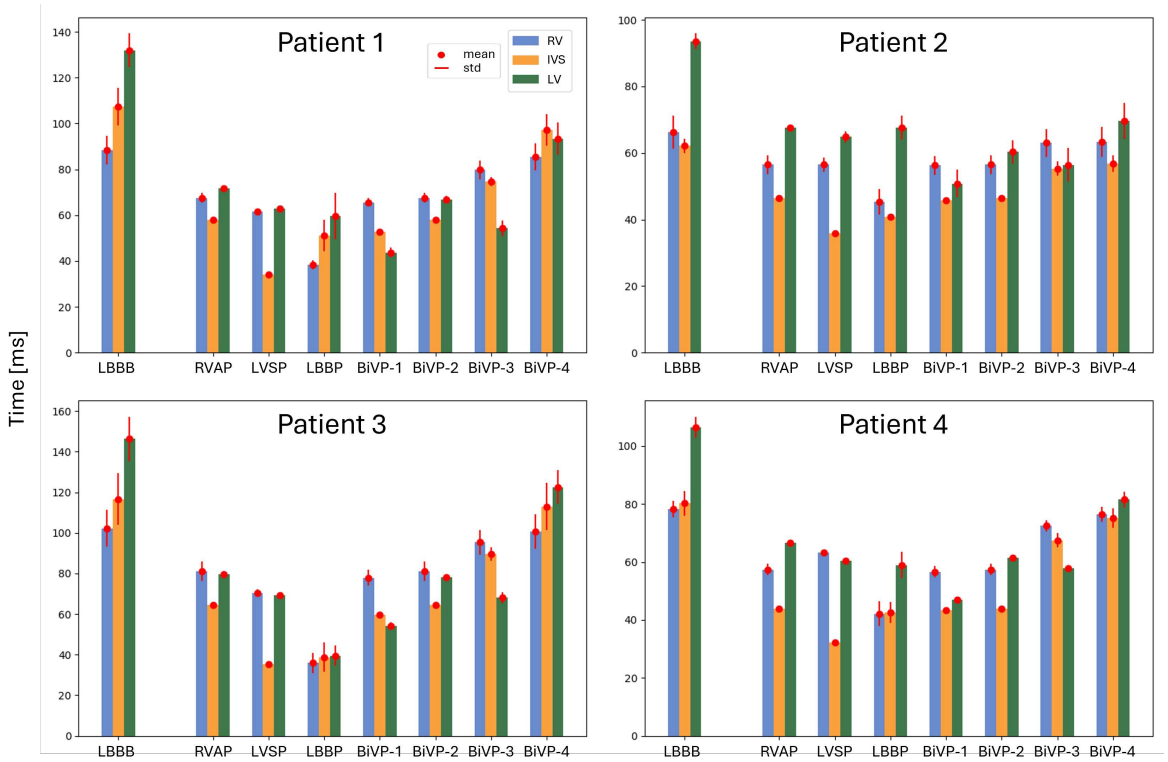

Figure 6: Mean and standard deviation of the activation time for the RV (blue), IVS (yellow), and LVfw (green) over the N_{sample} samples for the 4 patients.

the different pacing strategies, highlighting differences in contractile response between chambers. Data are shown as mean (red dots) ± standard deviation (red lines) over all N_{sample} samples. Despite the variability observed in electrical activation patterns for some pacing configurations, this variability does not translate into comparable differences in global hemodynamic metrics. The LV exhibits variations in contractile response that are comparable in magnitude to those observed clinically, whereas the RV shows smaller changes across strategies. For both ventricles, standard deviations are negligible in all patients, indicating that variability in the electrical activation patterns associated with a given pacing configuration has virtually no effect on the selected hemodynamic metrics. Accordingly, the reported differences primarily reflect the pacing strategy itself rather than the specific posterior activation sample.

Overall, these results highlight the strongly patient-specific nature of the acute response to CRT, with different pacing strategies yielding distinct trade-offs across electrophysiological and hemodynamic metrics. At the same time, the limited variability observed across posterior samples indicates that predicted hemodynamic outcomes are robust with respect to uncertainty in electrical activation.

3 Discussion

In this work, we presented a patient-specific computational framework for simulating cardiovascular function in the presence of ventricular conduction disturbances and their treatment via CRT. The proposed pipeline integrates an Eikonal-based electrophysiological model with a closed-loop cardiovascular model (CircAdapt), calibrated using Constrained Bayesian Optimization from non-invasive clinical data. Key features of the framework are its computational efficiency and its fully probabilistic formulation for parameter calibration, in which uncertainty is explicitly quantified and propagated throughout the pipeline. This enables both statistical characterization of inferred parameters and robust *in silico* evaluation of alternative therapeutic strategies.

From a computational standpoint, the framework is efficient and scalable. The cost of a single end-to-end simulation, comprising Purkinje network generation, Eikonal problem solution, and CircAdapt convergence, ranges from approximately 54 s to 76 s across the four patients (Table 1). While not real-time, this per-simulation cost enables the use of iterative optimization strategies such as CBO within clinically feasible time frames. Moreover, these timings are obtained using a non-optimized implementa-

	Patient 1				Patient 2			
	δ_{LV} [ms]	δ_{fw} [ms]	SLD [ms]	IVD [ms]	δ_{LV} [ms]	δ_{fw} [ms]	SLD [ms]	IVD [ms]
LBBB	17.71	14.46	97.23	30.70	21.04	14.83	109.42	10.83
RVAP	23.39	22.43	118.61	-3.09	20.52	18.65	105.21	0.15
LVSP	19.61	14.19	96.43	-14.04	19.76	13.44	97.67	-6.78
LBBP	12.46	11.97	72.25	16.76	18.72	13.11	99.61	8.39
BiVP-1	16.48	13.41	73.18	-17.18	15.11	13.88	77.30	-8.08
BiVP-2	20.86	18.07	102.71	-5.49	17.23	14.86	88.22	-3.38
BiVP-3	19.28	20.57	57.85	-14.62	13.01	14.52	66.37	-7.21
BiVP-4	14.35	13.07	69.39	9.95	14.23	12.32	75.56	-0.42
	Patient 3				**Patient 4**			
	δ_{LV} [ms]	δ_{fw} [ms]	SLD [ms]	IVD [ms]	δ_{LV} [ms]	δ_{fw} [ms]	SLD [ms]	IVD [ms]
LBBB	20.69	16.62	101.50	33.47	21.18	18.30	113.01	20.76
RVAP	25.69	24.52	130.09	-6.80	22.46	20.34	113.34	2.76
LVSP	21.83	14.69	101.94	-13.19	19.88	16.36	95.66	-10.85
LBBP	12.28	12.99	67.57	3.29	15.25	12.84	92.12	12.20
BiVP-1	17.42	14.95	87.40	-21.61	14.76	12.99	76.90	-10.76
BiVP-2	24.35	22.66	121.48	-7.82	18.45	15.62	97.67	-0.96
BiVP-3	22.23	22.61	72.01	-19.51	16.60	17.64	62.29	-11.98
BiVP-4	14.46	13.78	80.97	18.36	14.15	12.29	74.66	3.16

Table 4: Electrophysiological metrics used to quantify dyssynchrony for the different pacing strategies in the four patients. δ_{LV} and δ_{fw} denote the temporal dispersion of activation in the whole left ventricle and in the left ventricular free wall, respectively; SLD is the septal-to-lateral delay; and IVD is the interventricular delay. Green cells identify values satisfying the clinically consistent thresholds defined in Section 4.5.4.

tion and standard hardware. In particular, the Eikonal solver reported in Table 1 can be accelerated by at least one order of magnitude on modern GPU architectures, further supporting the scalability of the proposed approach.

The synthetic recovery test provides empirical evidence that the calibration procedure can recover parameters within the identifiable subset in the presence of measurement noise. The most identifiable parameters were recovered with mean relative errors between 5.5 % and 9.7 %, consistent with the limited information content of the calibration targets.

These findings are corroborated by the identifiability analysis. The condition numbers of the reduced sensitivity matrix remained below 10^3 for all patients, both at baseline and at the calibrated optimum, indicating acceptable local conditioning of the identifiable parameter subsets. Importantly, the set of identifiable parameters was patient-specific, highlighting the need for systematic sensitivity analysis when calibrating complex cardiovascular models. A moderate increase in the condition number was observed after calibration, reflecting the tendency of the optimization process to move toward regions of the parameter space with stronger parameter correlations.

Calibration errors on patient data were generally moderate, with three out of four patients exhibiting mean relative errors below 15 %. The higher error observed in Patient 3 (23 %) is likely related to the markedly dilated ventricular geometry, highlighting potential limitations of the model in cases of severe remodeling. A key observation is that variability across posterior samples has limited impact on the calibration outcome, indicating weak sensitivity to the specific activation pattern. This suggests that a single representative activation sample may be sufficient for practical calibration, without significantly affecting parameter estimates or model outputs.

This behavior is consistent with the robustness of the hemodynamic predictions observed across posterior samples, including after CRT simulations with different pacing strategies. Even in the case of conduction system pacing (CSP), where larger uncertainties are expected due to limited identifiability of the left Purkinje network from the ECG (e.g., LBBP in Fig. 5, where the standard deviation in LV

	Patient 1					Patient 2				
	ESV [mL]	EF [%]	MAP [mmHg]	max $\frac{dP}{dt}$ [$\frac{mmHg}{ms}$]	SW [mmHg mL]	ESV [mL]	EF [%]	MAP [mmHg]	max $\frac{dP}{dt}$ [$\frac{mmHg}{ms}$]	SW [mmHg mL]
LBBB	105.0	34.0	0.5	0.3	1575.6	113.7	35.8	3.1	0.8	6992.5
RVAP	+0.7%	-0.4%	-3.3%	-5.2%	-0.1%	-0.8%	+0.6%	-4.6%	-0.7%	+0.2%
LVSP	-1.0%	+1.2%	-12.3%	-0.8%	+1.3%	-1.1%	+1.5%	-4.8%	+2.2%	+2.5%
LBBP	-0.3%	+0.9%	-6.4%	+0.4%	+1.7%	-1.6%	+1.6%	-4.6%	+2.2%	+1.8%
BiVP-1	-0.4%	+0.7%	-10.1%	-5.0%	+0.3%	-4.5%	+4.2%	-10.6%	+4.4%	+4.3%
BiVP-2	+0.0%	+0.2%	-7.3%	-3.6%	+0.1%	-3.4%	+3.1%	-8.5%	+3.0%	+3.1%
BiVP-3	+1.0%	-0.3%	+0.0%	-6.7%	+0.5%	-4.7%	+4.6%	-10.1%	+4.8%	+4.9%
BiVP-4	-0.1%	+0.6%	-2.8%	-1.1%	+1.0%	-4.4%	+4.3%	-8.6%	+5.1%	+4.6%

	Patient 3					Patient 4				
	ESV [mL]	EF [%]	MAP [mmHg]	max $\frac{dP}{dt}$ [$\frac{mmHg}{ms}$]	SW [mmHg mL]	ESV [mL]	EF [%]	MAP [mmHg]	max $\frac{dP}{dt}$ [$\frac{mm_{Hg}}{ms}$]	SW [mmHg mL]
LBBB	117.1	32.3	5.4	1.5	11010.9	97.2	37.9	2.7	1.1	6270.6
RVAP	-1.6%	-1.1%	-5.6%	-3.1%	-6.5%	-1.7%	-1.7%	+1.0%	-4.2%	-8.9%
LVSP	+0.7%	+2.2%	+1.0%	+6.1%	+8.0%	-3.3%	+1.3%	+0.5%	+1.0%	-2.6%
LBBP	+1.4%	+4.8%	+5.5%	+12.5%	+18.1%	-8.4%	+3.9%	-9.5%	+2.7%	-4.6%
BiVP-1	-5.3%	+4.2%	-6.6%	+4.4%	+1.8%	-9.7%	+5.6%	-9.4%	+5.6%	-2.4%
BiVP-2	-2.5%	+0.0%	-6.0%	-1.9%	-5.1%	-6.1%	+2.4%	-6.6%	+1.5%	-4.5%
BiVP-3	+2.2%	+1.5%	+2.8%	+5.0%	+8.7%	-8.3%	+6.3%	-11.5%	+7.8%	+2.9%
BiVP-4	-2.6%	+4.7%	-0.7%	+8.7%	+9.0%	-8.0%	+6.9%	-14.1%	+9.1%	+6.0%

Table 5: Absolute values at the LBBB baseline (shaded rows) and relative changes for each pacing strategy with respect to LBBB. Relative changes are reported as signed percentages. Negative changes in ESV and MAP and positive changes in EF, max dP/dt, and SW indicate improved cardiac performance. Green cells identify the most favorable value for each metric within each patient.

activation reaches up to 20 ms), the variability in hemodynamic indices remains limited, as shown in Fig. 7. These results indicate that the dominant determinants of pump function are effectively captured by the calibrated model, and that uncertainty in the electrophysiological component has limited impact on clinically relevant outputs.

The electrophysiological analysis indicates that optimal electrical resynchronization is not solely determined by the pacing configuration, and no single strategy consistently improves all electrophysiological indices associated with favorable CRT response. This is evident in Table 4, where pacing strategies producing optimal activation patterns in one patient do not necessarily yield the same benefit in others. Among the investigated strategies, both left bundle branch pacing (LBBP) and biventricular pacing with delays applied to both leads (BiVP-4) generally result in the most synchronous electrical activation. However, the optimal strategy remains patient-specific. In Patient 2, for example, all pacing modalities lead to only limited reductions in activation delays and dispersion, and LBBP does not improve synchrony. This behavior is consistent with the presence of extensive scar tissue in the LV endocardium, which has been shown to disrupt the relationship between electrical activation and mechanical response even when located remotely from late-activated regions [38, 32].

The patient-specific nature of the acute response to CRT is even more apparent in the analysis of hemodynamic biomarkers. While all pacing configurations improve left ventricular performance relative to the LBBB baseline, no single modality consistently optimizes all metrics. For instance, pacing strategies yielding the largest gains in contractility do not necessarily correspond to the largest reductions in filling pressures. This dissociation suggests that optimizing CRT based on a single biomarker may be insufficient to fully characterize its hemodynamic benefit. Both the order of magnitude and the pattern of the improvements are consistent with clinical evidence from acute hemodynamic studies and randomized trials comparing different pacing strategies in patients with LBBB [39, 40, 41], further supporting the clinical plausibility of the patient-specific responses reproduced by our model. It is important to note that these results reflect only the acute response. The current model does not capture long-term adaptation processes such as reverse remodeling, which represent a clinically relevant outcome and may further differentiate pacing strategies over time.

Some limitations should be acknowledged. The present study is based on a small cohort and focuses on

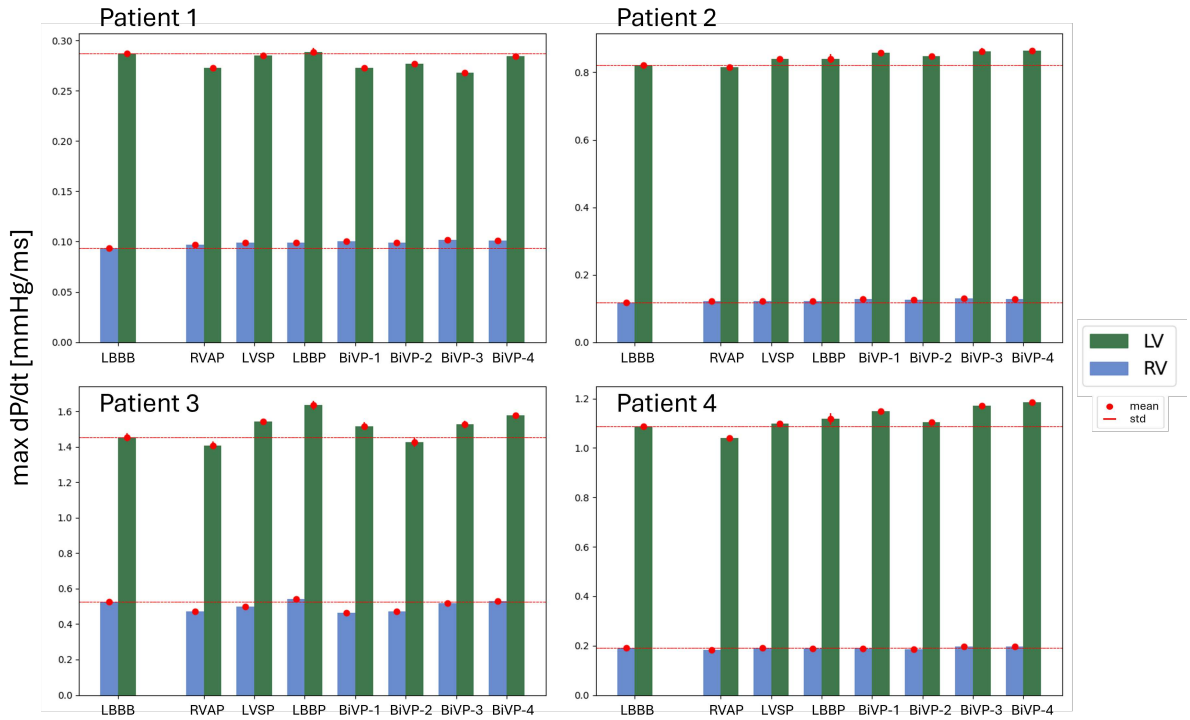

Figure 7: Maximum rate of pressure change for LV (green) and RV (blue) for all pacing strategies. Data are reported as mean (red dots) ± standard deviation (red lines) over all N_{sample} samples.

acute hemodynamic response, and the model relies on simplified mechanical assumptions. The proposed pipeline represents a computationally efficient compromise between fully coupled 3-D electromechanical models and reduced-order approaches aimed at capturing the dominant hemodynamic effects of CRT [16, 29]. Compared to the latter, the proposed framework does not require an anatomy-dependent offline training phase and retains full mechanistic interpretability.

Overall, these results further motivate the use of patient-specific computational models to explore multiple pacing strategies in a controlled setting. The proposed framework provides such a setting, being computationally efficient, patient-specific, calibrated on non-invasive data, and uncertainty-aware. The robustness of the predicted hemodynamic outcomes with respect to electrophysiological uncertainty, together with the low computational cost, supports the potential of this framework as a scalable and clinically applicable tool for personalized CRT planning.

4 Methods

4.1 Forward electrophysiology model

To simulate the mechanical and hemodynamic outcomes of conduction disorders and CRT, we first model the electrical activation in the reconstructed ventricles of patients. We employ an Eikonal model [26], which computes the activation time at each point by following the fastest propagation path from the initiation sites of electrical activation. The resulting simulations produce three-dimensional activation maps, which serve as inputs to the mechanical model.

Since electrical activation propagates faster along cardiac fibers than in the transverse direction, a fiber orientation field is generated using a rule-based algorithm [42]. The Purkinje network is identified using a probabilistic approach based on non-invasive clinical data, following [20]; further details are provided in Section 4.4.2.

4.1.1 Purkinje network parametrization

A parametric representation of the Purkinje network is generated using fractal trees [43]. To replicate the physiological structure of the conduction system, a root node is defined, together with an initial

direction and length, to initiate the main bundles. An arbitrary number of fascicles, each characterized by specific branching angles and lengths, are then generated. A fractal tree is grown from the end of each fascicle according to a predefined growth rule.

4.1.2 The Eikonal model

To simulate the ECG using a fast Eikonal-based solver, the Purkinje network is coupled to the myocardium at Purkinje–Myocardium Junctions (PMJs) located on the endocardial surface.

Let $\mathcal{P} = \cup_{k=1}^{N} \Gamma_k$ denote a Purkinje tree, where each branch Γ_k is a smooth open curve in $\mathbb{R}^3$. The nodes of the tree, denoted by p_i, define the boundary $\partial\mathcal{P} = \{p_i\}_{i=0}^{M}$, where p_0 is the root node, $\{p_i\}_{i=0}^{M_t}$ are the terminal PMJs, and $\{p_i\}_{i=M_t+1}^{M}$ are branching points. Let $\Omega \subset \mathbb{R}^3$ be a smooth domain representing the myocardium, with $p_i \in \partial\Omega$ for $i = 1, \dots, M_t$.

The travel time from the root node to the rest of the tree, denoted by $\tau^{\mathcal{P}} : \overline{\mathcal{P}} \to \mathbb{R}$, and the activation time in the myocardium, $\tau^{\mathcal{M}} : \Omega \to \mathbb{R}$, are obtained by solving the following system:

$$\begin{cases} c^{\mathcal{P}}(x)\,|\nabla\tau^{\mathcal{P}}(x)\cdot t(x)| = 1, & x \in \mathcal{P}, \\ \tau^{\mathcal{P}}(p_0) = t_0, & \\ \tau^{\mathcal{P}}(p_i) = \min\{\tau^{\mathcal{M}}(p_i), \tau^{\mathcal{P}}(p_i)\}, & p_i \in \partial\mathcal{P},\ i = 1, \dots, M_t, \\ \tau^{\mathcal{P}}(p_i) = \min\{\tau^{\mathcal{P}}|_{\partial\mathcal{P}}(p_i)\}, & i = M_t+1, \dots, M, \end{cases} \tag{1}$$

which governs activation in the Purkinje network. Here, $c^{\mathcal{P}} : \mathcal{P} \to \mathbb{R}$ and t denote the conduction velocity field and the tangent field along the Purkinje tree, respectively. The first two equations correspond to the Eikonal equation and the boundary condition at the root node. The third term represents the bidirectional coupling between the Purkinje tree and the myocardium at the PMJs: activation can propagate from the tree to the myocardium (orthodromic conduction) or from the myocardium to the tree (antidromic conduction). The last term enforces continuity at branching points.

For the myocardium, the activation time satisfies:

$$\begin{cases} \sqrt{\nabla\tau^{\mathcal{M}}(x)^{\top} D^{\mathcal{M}}(x)\,\nabla\tau^{\mathcal{M}}(x)} = 1, & x \in \Omega, \\ \tau^{\mathcal{M}}(p_i) = \min\{\tau^{\mathcal{M}}(p_i), \tau^{\mathcal{P}}(p_i)\}, & p_i \in \partial\mathcal{P},\ i = 1, \dots, M_t, \end{cases} \tag{2}$$

where $D^{\mathcal{M}} : \Omega \to \mathbb{R}^{3\times 3}$ is the conductivity tensor field, defined as in [26].

The coupled problem (1)–(2) is well-posed and admits a unique viscosity solution for any choice of the initial root time. Further details on the model and its numerical implementation are provided in [20].

The surface ECG is computed using a lead-field formulation [26]. Given the lead fields $Z_l(x) : \Omega \to \mathbb{R}$ for $l = 1, \dots, 12$, the l-th ECG lead is defined as:

$$V_l(t) = \int_{\Omega} \mathbf{G}_i(x)\,\nabla U\big(t - \tau^{\mathcal{M}}(x)\big)\cdot\nabla Z_l(x)\,\mathrm{d}x, \tag{3}$$

where $U(\xi)$ is a template action potential and $\mathbf{G}_i$ is the intracellular conductivity tensor.

4.2 Forward mechanics and hemodynamic model

The CircAdapt computational model of the human heart and circulation is used to simulate cardiovascular function. CircAdapt is a nonlinear 0D closed-loop ODE model of cardiovascular mechanics and hemodynamics, enabling nearly real-time simulation of cardiovascular physiology and pathophysiology, which is particularly advantageous for iterative personalization. CircAdapt has been extensively validated in previous studies [27, 44, 45, 46].

The cardiovascular system is represented as a concatenation of modules describing large compliant vessels, actively contracting chambers, valves, and the systemic and pulmonary peripheral circulation. The heart is modeled as five walls: the left and right atrial walls, the left and right ventricular walls, and the interventricular septum.

The MultiPatch module subdivides each cardiac wall into a finite number of patches, each characterized by its own stress–strain relationship for the constituent myofibers. Each patch is assumed to behave as part of a spherical wall with isotropic wall tension. As a consequence of this assumption, wall tension is homogeneous within each wall according to Laplace's law, and all patches behave as elements in series. Therefore, the spatial location of a patch does not affect the calculation of stress and strain; however, in

the presence of asynchronous activation, the patch location determines the activation timing, which in turn governs fiber stress and strain.

In this work, the MultiPatch module is implemented from scratch in a C++ version of CircAdapt, developed at the Medical University of Graz and largely based on the original MATLAB implementation [44]. The MultiPatch approach is applied to the ventricles only, while the atria are modeled using the original CircAdapt formulation, as activation times are available only for the ventricles from the electrophysiological model.

Further details on the governing equations of CircAdapt are provided in Appendix B.

4.3 EP–circulation coupling

The RV, LVfw, and IVS are subdivided according to the AHA segmentation [47]. The resulting segments, referred to as *patches*, are obtained using the universal ventricular coordinates (UVC) introduced in [48]. The UVC provide a global positioning system for three-dimensional biventricular heart geometries; their computation is outlined in Appendix A.

The activation time for each patch is defined as the mean electrical activation time of all nodes within the corresponding region. These region-averaged activation times are used as inputs to CircAdapt to drive patch-level mechanical activation. A detailed description of the equations coupling electrical activation timing with mechanical contraction is provided in Appendix B.

4.4 Calibration

Model calibration is a critical step for achieving patient-specific simulations consistent with available clinical data. A key feature of our methodology is the separate parametrization of the electrophysiological and cardiovascular components.

In the electrophysiological model, the optimization is restricted to parameters that directly influence ECG morphology, enabling targeted personalization of the activation sequence prior to coupling with the hemodynamic model. This separation also facilitates uncertainty quantification by decoupling electrophysiological and hemodynamic sources of variability.

4.4.1 Bayesian optimization

In the EP model, calibration is formulated as an optimization problem and addressed using Bayesian Optimization (BO), which enables efficient exploration of complex, high-dimensional parameter spaces while limiting the number of model evaluations.

We consider the following minimization problem:

$$\theta_{\min} = \arg\min_{\theta} y(\theta), \tag{4}$$

where $y(\theta)$ denotes the loss function. BO approximates the objective function using a Gaussian Process (GP) surrogate model [31], defined as

$$y = f(\theta) + \varepsilon, \tag{5}$$

where f is the latent function to be inferred and $\varepsilon \sim \mathcal{N}(0, \sigma_n^2 I)$ represents Gaussian, uncorrelated noise with unknown variance σ_n^2, which is learned from the data. The latent function is assigned a zero-mean Gaussian Process prior:

$$f(\theta) \sim \mathcal{GP}\left(0, k(\theta, \theta'; \beta)\right), \tag{6}$$

where $k(\theta, \theta'; \beta)$ is a covariance kernel with hyperparameters β.

The optimization proceeds by first evaluating the model at an initial set of N samples $\{(\theta_i, y_i)\}_{i=1}^{N}$, where y_i measures the mismatch between simulated and observed data. At each iteration, the GP surrogate is trained on the available data to estimate the posterior mean $\mu(\theta)$ and standard deviation $\sigma(\theta)$.

An acquisition function $a(\mu(\theta), \sigma(\theta))$ is then used to select the next evaluation point θ_{N+1}, balancing exploration of uncertain regions and exploitation of promising areas of the parameter space. The next sample is obtained by solving:

$$\theta_{N+1} = \arg\max_{\theta} a\left(\mu(\theta), \sigma(\theta)\right). \tag{7}$$

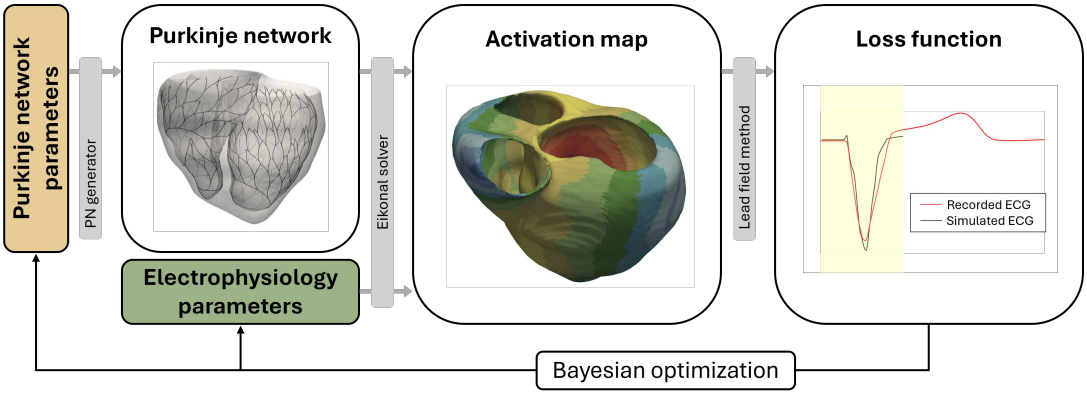

Figure 8: Schematic representation of the EP calibration workflow [20]. A parametric Purkinje network is generated in both ventricles. For a given network configuration and electrophysiological parameters, activation times are computed using the Eikonal model and the corresponding ECG is simulated. The simulated ECG is then compared with patient data, and the optimal parameters are estimated using Bayesian Optimization.

4.4.2 EP model calibration

The EP model is personalized by identifying the Purkinje network parameters that best reproduce the patient-specific ECG. A schematic overview of the calibration workflow is shown in Figure 8.

The calibration is formulated by defining a loss function that quantifies the mismatch between the simulated ECG and the observed data [34, 49]. The parameter vector θ includes both geometric parameters, such as fascicle lengths, branching angles, and initial bundle lengths, and electrophysiological parameters, including conduction velocity in the Purkinje network and the root activation time, which represents the delay between left and right Purkinje activation.

Let $\widehat{\mathbf{V}}(t)$ denote the reference 12-lead ECG and $\mathbf{V}(t;\theta)$ the simulated ECG. The loss function is defined in a least-squares sense as:

$$y(\theta) = \frac{1}{T}\int_0^T \left(\widehat{\mathbf{V}}(t) - \mathbf{V}(t;\theta)\right)^2 \, \mathrm{d}t, \tag{8}$$

where T is the QRS duration, corresponding to ventricular activation.

The minimization problem in Eq. (4) is solved using the BO framework described in Section 4.4.1. In each simulation, an initial set of 250 samples is generated using Latin Hypercube Sampling (LHS), followed by 300 BO iterations. Further details on the kernel, acquisition function, and optimization procedure are provided in [20].

Once the optimal parameters $\theta_{\min}$ are identified, a posterior distribution over the parameter space is estimated using Approximate Bayesian Computation (ABC) [18]. The Gaussian Process surrogate of the loss function is used to define the prior:

$$p(\theta) = \frac{1}{\sqrt{2\pi\,(\sigma^2(\theta) + \sigma^2_{\min})}} \exp\left(-\frac{1}{2}\frac{(\mu(\theta) - y_{\min})^2}{(\sigma^2(\theta) + \sigma^2_{\min})}\right), \tag{9}$$

where $y_{\min}$ and $\sigma^2_{\min}$ are the mean and variance predicted by the surrogate model at $\theta_{\min}$.

The ABC algorithm is then used to generate $N_{\text{sample}} = 30$ posterior samples. Each sampled parameter set corresponds to a distinct Purkinje network configuration and associated activation map consistent with the observed ECG. The resulting activation maps are averaged over predefined regions to obtain inputs for the mechanical model. This probabilistic formulation allows multiple activation patterns consistent with the same ECG to be retained, enabling uncertainty quantification.

In what follows, simulations based on these posterior activation maps are referred to as *LBBB simulations*.

4.4.3 Constrained Bayesian optimization

The calibration of CircAdapt is formulated as a constrained optimization problem, in which the optimal value of the loss function must correspond to a feasible parameter configuration, i.e., a set of parameters

for which the simulation successfully converges. Consequently, the acquisition function must account not only for expected improvement in model performance, but also for the likelihood of simulation feasibility.

To this end, we employ a constrained Bayesian optimization framework based on two separate surrogate models [30]. The objective function is modeled using a Gaussian Process (GP) regression trained exclusively on feasible evaluations. Parameter configurations leading to simulation failure are treated as infeasible and excluded from updates of the objective GP. For numerical stability, such failed simulations are assigned a large penalty value, which serves solely as a computational placeholder and does not influence the surrogate model.

In addition to the objective surrogate, feasibility is modeled using a dedicated GP surrogate. Rather than directly modeling a binary feasibility indicator, we introduce a real-valued latent feasibility function $g(\theta)$, learned through GP regression. Observed feasibility is encoded through a continuous proxy variable [50], enabling the use of standard GP regression while providing a smooth representation of feasibility across the parameter space.

Under this formulation, positive values of $g(\theta)$ correspond to regions that are likely to be feasible, whereas negative values indicate infeasibility. Given the GP posterior predictive distribution of $g(\theta)$, characterized by mean $\mu_c(\theta)$ and standard deviation $\sigma_c(\theta)$, the probability of feasibility at a candidate point θ is estimated as

$$\mathbb{P}[\text{feasible at } \theta] = \mathbb{P}\big[g(\theta) \geq 0\big] = \Phi\left(\frac{\mu_c(\theta)}{\sigma_c(\theta)}\right), \tag{10}$$

where $\Phi(\cdot)$ denotes the cumulative distribution function of the standard normal distribution.

Once both surrogate models are trained, the posterior predictive mean and standard deviation of the objective function, $(\mu_f(\theta), \sigma_f(\theta))$, are combined with the feasibility surrogate to define a constrained acquisition function. Specifically, we employ the constrained expected improvement (EI) criterion,

$$a(\theta) = \mathrm{EI}\left(\mu_f(\theta), \sigma_f(\theta)\right) \mathbb{P}\big[g(\theta) \geq 0\big], \tag{11}$$

which balances expected improvement over the current best feasible solution with the probability that the simulation remains feasible at the proposed parameter values.

4.4.4 CircAdapt model calibration

For each patient, the CircAdapt model is calibrated to match six measurements derived from CMR, corresponding to model outputs: left and right ventricular end-diastolic and end-systolic volumes, and left and right atrial end-diastolic volumes. These measurements, together with patient demographic data, are reported in Table 7 (Section 4.5.1). The overall calibration pipeline is outlined in Figure 9.

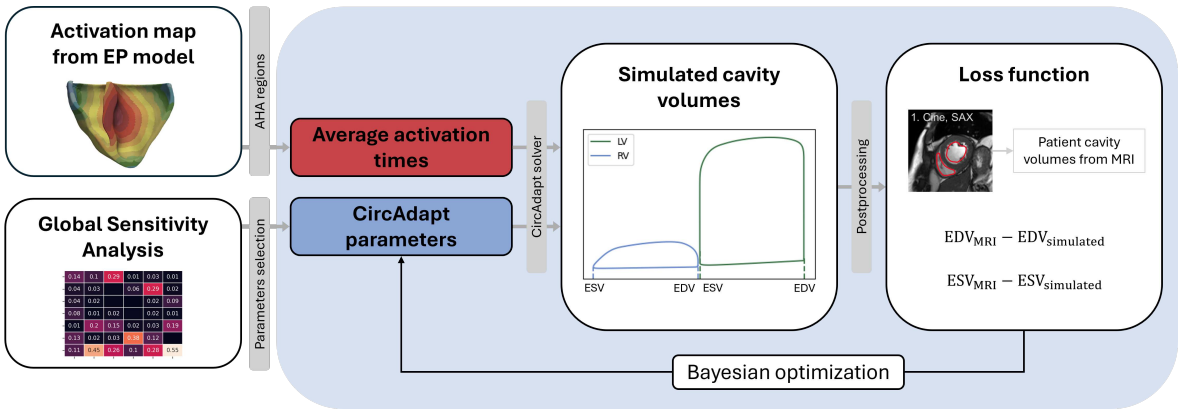

Figure 9: Calibration workflow for the CircAdapt model. Region-averaged activation times obtained from the EP model are used as inputs to CircAdapt. A global sensitivity analysis (GSA) is first performed to identify the parameters most influencing the target outputs. These parameters are then calibrated using Bayesian Optimization (BO, light blue block). Simulated end-diastolic and end-systolic volumes are compared with patient-specific CMR measurements.

We first perform a global sensitivity analysis (GSA) to identify the input parameters that most strongly affect the six target outputs. The analysis is carried out using the SALib library [51] with the

Sobol method [35]. The parameters considered in the GSA, together with those fixed to patient-specific values, are reported in Table 6.

Patient-specific inputs include the cardiac cycle length t_{cycle}, computed as the average interval between consecutive R-peaks in the ECG, the initial cavity volumes $V_{\text{c}} = \text{EDV}$, and the ventricular wall volumes V_v^{wall}, derived from the discretized anatomical models for the LV free wall (LVfw), septum, and RV free wall (RVfw). The activation delay $\Delta t_{\text{c}}^{\text{act}}$ is defined as the mean activation time within each patch from the LBBB simulations. For both the GSA and subsequent calibration, activation times are taken from a single representative sample among the N_{sample} posterior realizations.

The remaining parameters are varied within physiological ranges around their baseline values (Table 6), derived from experimental data [27]. The GSA is performed separately for each patient. Based on the Sobol total indices, a subset of N_{sa} influential parameters is selected by retaining those with total-order index greater than 0.1. The corresponding Sobol indices are reported in Appendix C. A further reduction to a subset of N_p parameters is performed through local identifiability analysis (Section 4.4.5).

Parameter	**Unit**	**Value**	**Description**	**Equation**
General				
q^{rest}	$\text{mL}\,\text{s}^{-1}$	85	Mean systemic flow at rest	(B.38)
t_{cycle}	s	ECG	Cardiac cycle length	(B.24)
Vessels				
$p_{\text{AO}}^{\text{ref}}$	kPa	12	Aortic reference pressure	(B.36)
$p_{\text{AP}}^{\text{ref}}$	kPa	1.8	Pulmonary artery reference pressure	(B.36)
$p_{\text{VC}}^{\text{ref}}$	kPa	0.12	Vena cava reference pressure	(B.36)
$p_{\text{VP}}^{\text{ref}}$	kPa	0.5	Pulmonary vein reference pressure	(B.36)
k_{a}	—	8	Arterial stiffness exponent	(B.35)
k_{v}	—	10	Venous stiffness exponent	(B.35)
$l_{\text{t}}^{\text{AO,VC}}$	mm	400	Aortic and vena cava length	(B.32)
$l_{\text{t}}^{\text{AP,VP}}$	mm	200	Pulmonary artery and vein length	(B.32)
Chambers				
Δt_{AV}	s	0.15	Atrio-ventricular delay	(B.26)
V_{c}	mL	CMR	Initial cavity volume	(B.1)
$V_{\text{v}}^{\text{wall}}$	mL	CMR	Ventricular wall volumes	(B.1)
$V_{\text{LA}}^{\text{wall}}$	mL	12	LA wall volume	(B.1)
$V_{\text{RA}}^{\text{wall}}$	mL	7	RA wall volume	(B.1)
$\Delta t_{\text{c}}^{\text{act}}$	s	EP model	Onset of activation	(B.26)
Sarcomeres				
$\sigma_{\text{v}}^{\text{act,max}}$	kPa	120	Maximal ventricular isometric stress	(B.27)
$\sigma_{\text{a}}^{\text{act,max}}$	kPa	84	Maximal atrial isometric stress	(B.27)
$\sigma_{\text{v}}^{\text{pas,max}}$	kPa	22	Maximal ventricular passive stress	(B.29)
$\sigma_{\text{a}}^{\text{pas,max}}$	kPa	50	Maximal atrial passive stress	(B.29)
Periphery				
$\Delta p_{\text{sys}}^{\text{ref}}$	kPa	12	Systemic blood pressure drop	(B.38)
$\Delta p_{\text{pulm}}^{\text{ref}}$	kPa	1.5	Pulmonary blood pressure drop	(B.38)

Table 6: CircAdapt input parameters considered in the global sensitivity analysis (GSA). Parameters fixed to patient-specific values are highlighted in gray. Baseline values are taken from [27].

Calibration is then carried out in the reduced parameter space by solving the minimization problem in Eq. (4) using the constrained Bayesian Optimization (CBO) framework described in Section 4.4.3. The loss function is defined as

$$y(\theta) = \sum_{i=1}^{6} \left(\frac{\widehat{V}_i - V_i(\theta)}{V_i(\theta)} \right)^2 , \tag{12}$$

where $\widehat{V}_i$ are the measured volumes and $V_i(\theta)$ are the corresponding model outputs.

The Gaussian Process surrogate employs an Automatic Relevance Determination (ARD) Matérn-3/2 kernel [52], defined as

$$k(\theta, \theta'; \beta) = \sigma_f^2(1 + \sqrt{3}r)\exp\left(-\sqrt{3}r\right), \tag{13}$$

with hyperparameters $\beta = \{\sigma_f, l_1, \ldots, l_n\}$, where σ_f is the signal standard deviation and l_i are the length scales associated with each input dimension. Larger values of l_i correspond to reduced sensitivity along the i-th parameter direction. The distance metric is defined as

$$r = \sqrt{\sum_{i=1}^{n} \frac{(\theta_i - \theta_i^{'})^2}{l_i^2}}. \tag{14}$$

The surrogate model is initially trained using $N = 150$ samples generated via Latin Hypercube Sampling (LHS). The GP hyperparameters are estimated by maximizing the log marginal likelihood using the `minimize` function from SciPy [53], with a multi-start L-BFGS-B algorithm [54]. Input parameters are rescaled to the unit hypercube $[0, 1]^D$, while outputs are standardized to zero mean and unit variance.

Hyperparameters are constrained within predefined ranges to ensure numerical stability: the signal variance is restricted to $[10^{-2}, 10]$, length scales to $[10^{-2}, 0.5]$, and observation noise variance to $[10^{-6}, 10^{-2}]$. Optimization is performed in log-space to enforce positivity and improve robustness [52, 55]. The acquisition function is maximized using L-BFGS-B with 50 random restarts, and the BO procedure is run for 300 iterations.

4.4.5 CircAdapt model: local identifiability and synthetic recovery test

Parameter identifiability is first assessed prior to optimization. The local practical identifiability of the N_{sa} parameters selected from the GSA is evaluated using the normalized sensitivity matrix $S \in \mathbb{R}^{6\times N_{sa}}$, with entries

$$S_{i,j} = \frac{\partial V_i}{\partial \theta_j}\frac{\theta_j}{V_i}, \tag{15}$$

computed at the nominal parameter vector (Table 6) [56].

Since the number of candidate parameters exceeds the number of independent observables, only a subset can be locally identified. This subset is determined by applying a QR decomposition with column pivoting [57] to S. Parameters satisfying $R_{kk}/R_{11} < 10^{-3}$ are considered linearly dependent and excluded, yielding a reduced set of N_p locally identifiable parameters.

Calibration is then performed via BO in this reduced parameter space. At the identified optimum, identifiability is reassessed by analyzing the condition number $k = s_{\max}/s_{\min}$ of the reduced sensitivity matrix S_{red}, which provides a measure of local conditioning [56]. In addition, the Fisher Information Matrix (FIM) [58] is computed as

$$F = S_{\text{red}}^T S_{\text{red}}, \tag{16}$$

whose diagonal entries quantify parameter sensitivities and whose off-diagonal terms reflect parameter correlations under the available measurements.

The robustness of the calibration procedure is further evaluated through a synthetic recovery test on a representative patient. Ground-truth parameter values are used to generate model outputs, to which multiplicative Gaussian noise is added:

$$\tilde{V}_i = V_{i,\text{true}}(1 + \varepsilon_i), \quad \varepsilon_i \sim \mathcal{N}(0, \sigma^2), \quad i = 1, \ldots, 6, \tag{17}$$

with $\sigma = 0.05$ (5%), consistent with the inter-observer variability in CMR-derived cardiac volumes [59].

The noisy outputs are then used as targets in the BO procedure, and the recovered parameters are compared with the ground-truth values. The experiment is repeated 20 times with different random seeds to generate independent noise realizations.

4.5 Experimental setup

4.5.1 Patient data

We retrospectively investigated four heart failure patients with a left ventricular (LV) ejection fraction below 35%, NYHA class II–IV, and a QRS duration greater than 120 ms. All patients were candidates

for cardiac resynchronization therapy (CRT) device implantation and underwent standard 12-lead ECG and CMR imaging, including late gadolinium enhancement (LGE) for scar detection. The cavity volumes measured from CMR, together with demographic information, are reported in Table 7.

Clinical data and model construction have been previously described in [38, 34]. The study protocol was approved by the institutional review board, and all patients provided written informed consent. The study was conducted in accordance with the Declaration of Helsinki.

Patient-specific cardiac anatomies were semi-automatically reconstructed from CMR images. Surfaces of relevant anatomical structures were generated from segmented contours using Blender (Blender Foundation). Ventricular contours were derived from short-axis cine CMR images. Scar tissue was identified from LGE-MRI sequences via manual contouring and registration and defined as non-active myocardium in the forward EP model.

The cardiac anatomy was discretized into a three-dimensional volumetric grid with 1 mm spatial resolution. Ventricular fiber orientation was assigned using a rule-based method [42]. A 5-minute ECG was recorded using a clinically available system (CS200 excellence, Schiller AG), with a sampling rate of $1000\,\mathrm{s}^{-1}$ and an amplitude resolution of 1 µV.

	Patient 1	**Patient 2**	**Patient 3**	**Patient 4**
t_{cycle} [s]	0.92	0.93	0.93	0.72
Wall volumes [mL]				
$V_{\mathrm{LV}}^{\mathrm{wall}}$	63	74	131	83
$V_{\mathrm{IVS}}^{\mathrm{wall}}$	41	49	59	55
$V_{\mathrm{RV}}^{\mathrm{wall}}$	23	26	52	29
Cavity volumes [mL]				
$V_{\mathrm{LV}}^{\mathrm{ED}}$	138	178	216	145
$V_{\mathrm{LV}}^{\mathrm{ES}}$	84	124	143	80
$V_{\mathrm{RV}}^{\mathrm{ED}}$	75	107	173	106
$V_{\mathrm{RV}}^{\mathrm{ES}}$	26	35	96	47
$V_{\mathrm{LA}}^{\mathrm{ED}}$	50	86	84	79
$V_{\mathrm{RA}}^{\mathrm{ED}}$	50	78	70	63
Sex	F	M	M	M
Dil.	×	✓	✓	×
Scar	×	✓	×	×

Table 7: Patient demographics and CMR measurements. LV: left ventricle; RV: right ventricle; LA: left atrium; RA: right atrium; ED: end-diastole; ES: end-systole. Dil.: dilated heart.

4.5.2 Pacing protocols

For pacing simulations, different initiation sites are defined for each protocol, using the set of Purkinje networks obtained from the LBBB simulations (i.e., the N_{sample} networks resulting from the EP optimization). Pacing is simulated by assuming that all nodes within 2 mm of the pacing site act as sources of electrical activation.

Figure 10 illustrates the pacing sites considered in the myocardium. In right ventricular apical pacing (RVAP), the pacing site is located at the RV apical endocardium, while in biventricular pacing (BiVP) an additional site is placed on the LV free wall (LVfw) epicardium. The LV epicardial pacing site is defined as the location with the latest activation time in the LBBB simulations.

For BiVP, different delays between the two pacing leads are considered. BiVP-1 corresponds to simultaneous activation of both leads. In BiVP-2, a delay equal to the earliest ventricular activation time in the baseline (LBBB) condition is applied to the LV epicardial lead. In BiVP-3, the same delay is applied to the RV endocardial lead, while in BiVP-4 both leads are activated with a delay. In left ventricular septal pacing (LVSP), stimulation is applied at a selected septal location.

To model conduction system pacing (LBBP), where the pacemaker directly stimulates the Purkinje network to synchronize ventricular activation [60], the patient-specific Purkinje networks are used and

the root activation time is set to 0 ms, enforcing simultaneous activation of the left and right Purkinje trees.

In what follows, the term *EP simulations* refers to the set of eight simulations per sample, including the LBBB baseline and the seven pacing configurations.

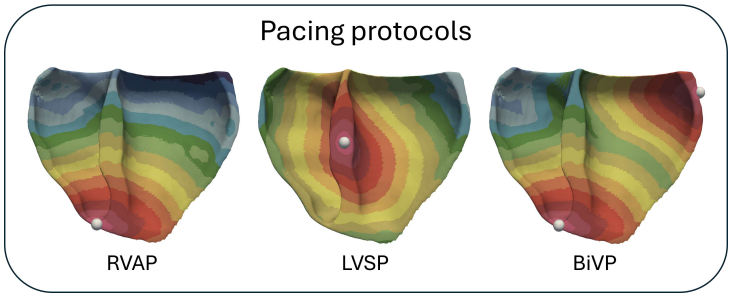

Figure 10: Pacing protocols. RVAP: right ventricular apical pacing; LVSP: left ventricular septal pacing; BiVP: biventricular pacing.

4.5.3 Simulation protocols

After CircAdapt calibration, a baseline simulation representing LBBB is performed for all N_{sample} sets of activation times for each patient. Subsequently, using the same calibrated parameters, different pacing scenarios are simulated by replacing the activation times with those obtained from the various pacing protocols. Hemodynamic variables from these simulations are then compared against the baseline LBBB configuration.

It is important to note that the CircAdapt model does not account for long-term changes in tissue properties associated with reverse remodeling, which is known to influence CRT outcomes. Therefore, in the pacing simulations, remodeling-related parameters (e.g., wall volumes) are kept fixed. This corresponds to modeling an acute scenario, representing the immediate hemodynamic response following device implantation.

4.5.4 Evaluation metrics

Electrophysiological (EP) metrics were selected to capture both local and regional characteristics of myocardial activation, while ensuring robustness with respect to inter-sample variability. Average activation times were computed for each patch in the AHA bullseye representation, reporting mean and standard deviation across the N_{sample} samples.

In addition, regional mean activation times were evaluated for all EP simulations by considering three myocardial regions: RV free wall (RVfw), interventricular septum (IVS), and left ventricular free wall (LVfw). For each simulation, activation times were first averaged over all patches within each region and then averaged across the N_{sample} samples.

Global activation patterns were quantified using complementary intraventricular and interventricular metrics. The septal-to-lateral delay (SLD) was used to assess intraventricular dyssynchrony [61]. The temporal dispersion of activation was quantified by the standard deviation δ of activation times within each region, with δ_{LV} and δ_{LVfw} representing dispersion in the entire left ventricle and in the LV free wall, respectively. Interventricular synchrony was assessed using the interventricular delay (IVD), defined as the difference between mean activation times in the LV and RV.

To identify pacing strategies associated with improved electrical synchrony, we considered reductions in activation dispersion and SLD, together with acceptable values of IVD, based on thresholds consistent with those reported in clinical studies of acute CRT response.

The effects of pacing on cardiac function were further quantified using mechanical and hemodynamic biomarkers commonly adopted in clinical practice [62]. The analysis focuses on left ventricular metrics, as the LV is the primary chamber affected by LBBB and the main target of CRT.

For each pacing configuration, we computed the mean relative variation across N_{sample} samples of end-systolic volume (ESV), ejection fraction (EF), mean atrial pressure (MAP), maximum rate of pressure rise ($\max \mathrm{d}P/\mathrm{d}t$), and stroke work (SW), all expressed with respect to the pathological LBBB baseline for each patient. Negative variations in ESV and MAP, together with positive variations in EF, $\max \mathrm{d}P/\mathrm{d}t$, and SW, indicate improved LV systolic performance and hemodynamic efficiency.

The maximum rate of pressure rise, $\max \mathrm{d}P/\mathrm{d}t$, provides a direct measure of myocardial contractile strength, reflecting the ability of the myocardium to generate active tension during isovolumetric contraction. In patients with LBBB and heart failure, $\max \mathrm{d}P/\mathrm{d}t$ is typically reduced due to delayed and inefficient activation. Owing to its sensitivity in the acute setting [8], this index is widely used to assess immediate CRT effects, with acute increases on the order of 10 % being associated with subsequent reverse remodeling [63].

Data availability

The clinical data used in this study consist of patient-specific ECG and CMR measurements and are subject to ethical and privacy restrictions; therefore, they are not publicly available.

Access to anonymized data may be considered upon reasonable request and subject to approval by the relevant institutional review board.

To facilitate reproducibility, a proof-of-concept dataset based on synthetic data can be provided upon reasonable request.

Code availability

The electrophysiological model and Bayesian optimization framework used for Purkinje network inference are available from previous work [20].

The constrained Bayesian optimization (CBO) framework and the coupling pipeline between electrophysiology and circulation models can be made available upon reasonable request to the corresponding author.

The CircAdapt implementation used in this study is based on a C++ version of the model developed at the Medical University of Graz and is not publicly available. A proof-of-concept implementation of the pipeline, using an external CircAdapt interface, can be provided upon reasonable request.

A simplified example demonstrating the main steps of the pipeline can be shared for reproducibility purposes.

Funding

This work was supported by a scholarship funded by Ministerial Decree no. 118 of 2 March 2023, under the National Recovery and Resilience Plan (NRRP), financed by the European Union – NextGenerationEU – Mission 4, Investment 4.1.

S.P. acknowledges support from the PRIN2022 project (MUR, Italy, 2023–2025, no. P2022N5ZNP) "SIDDMs", funded by the European Union (NextGenerationEU, Mission 4, Component 2); the CSCS Swiss National Supercomputing Centre (project no. lp100); and the SNSF–FWF project "CardioTwin" (no. 214817).

F.S.C. acknowledges support from the FONDECYT Regular 1251394 project funded by ANID. This work was also supported by the ANID Millennium Science Initiative Program (ICN2021_004) and the National Center for Artificial Intelligence CENIA (FB210017, Basal ANID).

F.C. acknowledges support from the Land Steiermark UFO Grant No. 3026.

This research was funded in whole or in part by the Austrian Science Fund (FWF) [10.55776/P37063] to C.M.A.

E.B. F.C. and S.P. are members of GNCS (Gruppo Nazionale per il Calcolo Scientifico) of INdAM (Istituto Nazionale di Alta Matematica).

Author contributions

E.B. and S.P. conceived and designed the study. E.B., F.S.C., C.A., and S.P. contributed to code development. E.B. wrote the initial draft of the manuscript. E.B., F.C., and S.P. contributed to data analysis and interpretation, as well as critical revision of the manuscript for important intellectual content. All authors approved the final version of the manuscript.

Competing interests

The authors declare no competing financial or non-financial interests.

Ethics

The study protocol was approved by the relevant institutional review board. All participants provided written informed consent prior to inclusion in the study. The study was conducted in accordance with the Declaration of Helsinki.

References

[1] MO Sweeney and FW Prinzen. "Ventricular pump function and pacing: physiological and clinical integration". In: *Circulation: Arrhythmia and Electrophysiology* 1.2 (2008), pp. 127–139.

[2] ER Pfeiffer, JR Tangney, JH Omens, and AD McCulloch. "Biomechanics of cardiac electromechanical coupling and mechanoelectric feedback". In: *Journal of biomechanical engineering* 136.2 (2014), p. 021007.

[3] DG Strauss, RH Selvester, and GS Wagner. "Defining left bundle branch block in the era of cardiac resynchronization therapy". In: *The American journal of cardiology* 107.6 (2011), pp. 927–934.

[4] MO Sweeney and FW Prinzen. "A new paradigm for physiologic ventricular pacing". In: *Journal of the American College of Cardiology* 47.2 (2006), pp. 282–288.

[5] JG Cleland, N Freemantle, E Erdmann, D Gras, L Kappenberger, L Tavazzi, and JC Daubert. "Long-term mortality with cardiac resynchronization therapy in the Cardiac Resynchronization-Heart Failure (CARE-HF) trial". In: *European journal of heart failure* 14.6 (2012), pp. 628–634.

[6] ES Tan, R Soh, E Boey, JY Lee, J de Leon, SP Chan, HH Gan, SC Seow, and P Kojodjojo. "Comparison of pacing performance and clinical outcomes between left bundle branch and His bundle pacing". In: *Clinical Electrophysiology* 9.8_Part_1 (2023), pp. 1393–1403.

[7] L Gerra, N Bonini, DA Mei, JF Imberti, M Vitolo, T Bucci, G Boriani, and GY Lip. "Cardiac resynchronization therapy (CRT) nonresponders in the contemporary era: a state-of-the-art review". In: *Heart Rhythm* 22.1 (2025), pp. 159–169.

[8] DD Spragg, J Dong, BJ Fetics, R Helm, JE Marine, A Cheng, CA Henrikson, DA Kass, and RD Berger. "Optimal left ventricular endocardial pacing sites for cardiac resynchronization therapy in patients with ischemic cardiomyopathy". In: *Journal of the American College of Cardiology* 56.10 (2010), pp. 774–781.

[9] C Rodero, TM Baptiste, RK Barrows, A Lewalle, SA Niederer, and M Strocchi. "Advancing clinical translation of cardiac biomechanics models: a comprehensive review, applications and future pathways". In: *Frontiers in physics* 11 (2023), p. 1306210.

[10] RC Kerckhoffs, JH Omens, and AD McCulloch. "Mechanical discoordination increases continuously after the onset of left bundle branch block despite constant electrical dyssynchrony in a computational model of cardiac electromechanics and growth". In: *Europace* 14.suppl_5 (2012), pp. v65–v72.

[11] J Constantino, Y Hu, AC Lardo, and NA Trayanova. "Mechanistic insight into prolonged electromechanical delay in dyssynchronous heart failure: a computational study". In: *American Journal of Physiology-Heart and Circulatory Physiology* 305.8 (2013), H1265–H1273.

[12] AW Lee, CM Costa, M Strocchi, CA Rinaldi, and SA Niederer. "Computational modeling for cardiac resynchronization therapy". In: *Journal of cardiovascular translational research* 11 (2018), pp. 92–108.

[13] P Bhagirath, M Strocchi, MJ Bishop, PM Boyle, and G Plank. "From bits to bedside: entering the age of digital twins in cardiac electrophysiology". In: *Europace* 26.12 (2024), euae295.

[14] E Sung, A Prakosa, S Zhou, RD Berger, J Chrispin, S Nazarian, and NA Trayanova. "Fat infiltration in the infarcted heart as a paradigm for ventricular arrhythmias". In: *Nature cardiovascular research* 1.10 (2022), pp. 933–945.

[15] M Strocchi, JW Samways, A Naraen, N Ali, MJ Shun-Shin, K Gillette, CA Rinaldi, AD Arnold, G Plank, EJ Vigmond, et al. "An in silico guide for ventriculo-ventricular delay programming for left bundle branch-optimized cardiac resynchronization therapy". In: *Europace* 27.5 (2025), euaf089.

[16] CM Augustin, MA Gsell, E Karabelas, E Willemen, FW Prinzen, J Lumens, EJ Vigmond, and G Plank. "A computationally efficient physiologically comprehensive 3D–0D closed-loop model of the heart and circulation". In: *Computer methods in applied mechanics and engineering* 386 (2021), p. 114092.

[17] T Grandits, K Gillette, G Plank, and S Pezzuto. "Accurate and efficient cardiac digital twin from surface ECGs: Insights into identifiability of ventricular conduction system". In: *Medical Image Analysis* 105 (2025), p. 103641.

[18] M Sunnåker, AG Busetto, E Numminen, J Corander, M Foll, and C Dessimoz. "Approximate bayesian computation". In: *PLoS computational biology* 9.1 (2013), e1002803.

[19] R Meiburg, JH Rijks, AS Beela, E Bressi, D Grieco, T Delhaas, JGL Luermans, FW Prinzen, K Vernooy, and J Lumens. "Comparison of novel ventricular pacing strategies using an electro-mechanical simulation platform". In: *Europace* 25.6 (2023), euad144.

[20] F Álvarez-Barrientos, M Salinas-Camus, S Pezzuto, and FS Costabal. "Probabilistic learning of the Purkinje network from the electrocardiogram". In: *Medical Image Analysis* (2025), p. 103460.

[21] T Arts, T Delhaas, P Bovendeerd, X Verbeek, and FW Prinzen. "Adaptation to mechanical load determines shape and properties of heart and circulation: the CircAdapt model". In: *American Journal of Physiology-Heart and Circulatory Physiology* 288.4 (2005), H1943–H1954.

[22] J Lumens, T Delhaas, B Kirn, and T Arts. "Three-wall segment (TriSeg) model describing mechanics and hemodynamics of ventricular interaction". In: *Annals of biomedical engineering* 37 (2009), pp. 2234–2255.

[23] A Neic, FO Campos, AJ Prassl, SA Niederer, MJ Bishop, EJ Vigmond, and G Plank. "Efficient computation of electrograms and ECGs in human whole heart simulations using a reaction-eikonal model". In: *Journal of computational physics* 346 (2017), pp. 191–211.

[24] T Grandits, J Verhülsdonk, G Haase, A Effland, and S Pezzuto. "Digital twinning of cardiac electrophysiology models from the surface ECG: a geodesic backpropagation approach". In: *IEEE Transactions on Biomedical Engineering* 71.4 (2023), pp. 1281–1288.

[25] S Brunati, M Bucelli, R Piersanti, L Dede', and C Vergara. "Coupled Eikonal problems to model cardiac reentries in Purkinje network and myocardium". In: *SIAM Journal on Scientific Computing* 48.2 (2026), B184–B207.

[26] S Pezzuto, P Kal'avskỳ, M Potse, FW Prinzen, A Auricchio, and R Krause. "Evaluation of a rapid anisotropic model for ECG simulation". In: *Frontiers in physiology* 8 (2017), p. 265.

[27] J Walmsley, T Arts, N Derval, P Bordachar, H Cochet, S Ploux, FW Prinzen, T Delhaas, and J Lumens. "Fast simulation of mechanical heterogeneity in the electrically asynchronous heart using the multipatch module". In: *PLoS computational biology* 11.7 (2015), e1004284.

[28] G Plank, T Schrotter, M Gsell, E Zappon, C Augustin, A Neic, and S Pezzuto. "A Physics-Informed Eikonal Model for Simulating Arrhythmias in the Human Heart in Real-Time". In: *Research Square* (2025). preprint. DOI: 10.21203/rs.3.rs-7741556/v1.

[29] E Capuano, F Regazzoni, M Maines, S Fornara, V Locatelli, D Catanzariti, S Stella, F Nobile, MD Greco, and C Vergara. "Personalized computational electro-mechanics simulations to optimize cardiac resynchronization therapy". In: *Biomechanics and Modeling in Mechanobiology* 23.6 (2024), pp. 1977–2004.

[30] S Amini, I Vannieuwenhuyse, and A Morales-Hernández. "Constrained bayesian optimization: A review". In: *Ieee Access* 13 (2024), pp. 1581–1593.

[31] R Garnett. *Bayesian optimization*. Cambridge University Press, 2023.

[32] NJ Verzaal, CJ Van Deursen, S Pezzuto, L Wecke, WM Van Everdingen, K Vernooy, T Delhaas, A Auricchio, and FW Prinzen. "Synchronization of repolarization after cardiac resynchronization therapy: A combined clinical and modeling study". In: *Journal of Cardiovascular Electrophysiology* 33.8 (2022), pp. 1837–1846.

[33] T Koopsen, W Gerrits, N van Osta, T van Loon, P Wouters, FW Prinzen, K Vernooy, T Delhaas, AJ Teske, M Meine, et al. "Virtual pacing of a patient's digital twin to predict left ventricular reverse remodelling after cardiac resynchronization therapy". In: *Europace* 26.1 (2024), euae009.

[34] S Pezzuto, FW Prinzen, M Potse, F Maffessanti, F Regoli, ML Caputo, G Conte, R Krause, and A Auricchio. "Reconstruction of three-dimensional biventricular activation based on the 12-lead electrocardiogram via patient-specific modelling". In: *EP Europace* 23.4 (2021), pp. 640–647.

[35] IM Sobol. "Global sensitivity indices for nonlinear mathematical models and their Monte Carlo estimates". In: *Mathematics and computers in simulation* 55.1-3 (2001), pp. 271–280.

[36] VC Machado, G Tapia, D Gabriel, J Lafuente, and JA Baeza. "Systematic identifiability study based on the Fisher Information Matrix for reducing the number of parameters calibration of an activated sludge model". In: *Environmental Modelling & Software* 24.11 (2009), pp. 1274–1284.

[37] GH Golub and CF Van Loan. *Matrix computations*. JHU press, 2013.

[38] F Maffessanti, T Jadczyk, R Kurzelowski, et al. "The influence of scar on the spatio-temporal relationship between electrical and mechanical activation in heart failure patients". In: *EP Europace* 22.5 (2020), pp. 777–786. DOI: 10.1093/europace/euz346.

[39] M Jastrzębski, P Foley, B Chandrasekaran, Z Whinnett, P Vijayaraman, GA Upadhyay, RD Schaller, R Gardas, T Richardson, D Kudlik, et al. "Multicenter hemodynamic assessment of the LOT-CRT strategy: when does combining left bundle branch pacing and coronary venous pacing enhance resynchronization?: primary results of the CSPOT study". In: *Circulation: Arrhythmia and Electrophysiology* 17.11 (2024), e013059.

[40] P Paluszkiewicz, A Martuszewski, J Smereka, and J Gajek. "A Meta-Analysis of Clinical and Echocardiographic Outcomes of Physiological Versus Conventional Pacing". In: *Biomedicines* 13.6 (2025), p. 1359.

[41] N Inoue, S Morikawa, Y Ito, Y Takayama, T Hiramatsu, R Ohinata, D Okamoto, and T Murohara. "Evaluation of cardiac energetics in left bundle branch area pacing using noninvasive pressure–volume loops". In: *Heart Rhythm O2* 6.6 (2025), pp. 789–798.

[42] M Potse, D Krause, W Kroon, R Murzilli, S Muzzarelli, F Regoli, E Caiani, FW Prinzen, R Krause, and A Auricchio. "Patient-specific modelling of cardiac electrophysiology in heart-failure patients". In: *Europace* 16.suppl_4 (2014), pp. iv56–iv61.

[43] FS Costabal, DE Hurtado, and E Kuhl. "Generating Purkinje networks in the human heart". In: *Journal of biomechanics* 49.12 (2016), pp. 2455–2465.

[44] J Lumens and T Delhaas. "Cardiovascular modeling in pulmonary arterial hypertension: focus on mechanisms and treatment of right heart failure using the CircAdapt model". In: *The American journal of cardiology* 110.6 (2012), S39–S48.

[45] NH Kuijpers, E Hermeling, J Lumens, HM ten Eikelder, T Delhaas, and FW Prinzen. "Mechano-electrical coupling as framework for understanding functional remodeling during LBBB and CRT". In: *American Journal of Physiology-Heart and Circulatory Physiology* 306.12 (2014), H1644–H1659.

[46] PJ Oomen, TKN Phung, SH Weinberg, KC Bilchick, and JW Holmes. "A rapid electromechanical model to predict reverse remodeling following cardiac resynchronization therapy". In: *Biomechanics and modeling in mechanobiology* 21.1 (2022), pp. 231–247.

[47] AHAWG on Myocardial Segmentation, R for Cardiac Imaging: MD Cerqueira, et al. "Standardized myocardial segmentation and nomenclature for tomographic imaging of the heart: a statement for healthcare professionals from the Cardiac Imaging Committee of the Council on Clinical Cardiology of the American Heart Association". In: *Circulation* 105.4 (2002), pp. 539–542.

[48] J Bayer, AJ Prassl, A Pashaei, JF Gomez, A Frontera, A Neic, G Plank, and EJ Vigmond. "Universal ventricular coordinates: A generic framework for describing position within the heart and transferring data". In: *Medical image analysis* 45 (2018), pp. 83–93.

[49] S Pezzuto, P Perdikaris, and FS Costabal. "Learning cardiac activation maps from 12-lead ECG with multi-fidelity Bayesian optimization on manifolds". In: *IFAC-PapersOnLine* 55.20 (2022), pp. 175–180.

[50] MA Gelbart, J Snoek, and RP Adams. "Bayesian optimization with unknown constraints". In: *arXiv preprint arXiv:1403.5607* (2014).

[51] J Herman and W Usher. "SALib: An open-source Python library for sensitivity analysis". In: *Journal of Open Source Software* 2.9 (2017), p. 97.

[52] CK Williams and CE Rasmussen. *Gaussian processes for machine learning*. Vol. 2. MIT press Cambridge, MA, 2006.

[53] P Virtanen, R Gommers, TE Oliphant, M Haberland, T Reddy, D Cournapeau, E Burovski, P Peterson, W Weckesser, J Bright, et al. "SciPy 1.0: fundamental algorithms for scientific computing in Python". In: *Nature methods* 17.3 (2020), pp. 261–272.

[54] C Zhu, RH Byrd, P Lu, and J Nocedal. "Algorithm 778: L-BFGS-B: Fortran subroutines for large-scale bound-constrained optimization". In: *ACM Transactions on mathematical software (TOMS)* 23.4 (1997), pp. 550–560.

[55] J Snoek, H Larochelle, and RP Adams. "Practical bayesian optimization of machine learning algorithms". In: *Advances in neural information processing systems* 25 (2012).

[56] R Brun, P Reichert, and HR Künsch. "Practical identifiability analysis of large environmental simulation models". In: *Water Resources Research* 37.4 (2001), pp. 1015–1030.

[57] M Fink, A Attarian, and H Tran. "Subset selection for parameter estimation in an HIV model". In: *PAMM: Proceedings in Applied Mathematics and Mechanics*. Vol. 7. Wiley Online Library. 2007, pp. 1121501–1121502.

[58] F Caforio, G Montecinos, LO Muller, PJ Blanco, and EF Toro. "Assessment of reduced-order unscented Kalman filter for parameter identification in 1-dimensional blood flow models using experimental data". In: *International journal for numerical methods in biomedical engineering* 33.8 (2017), e2843.

[59] RH Davies, JB Augusto, A Bhuva, H Xue, TA Treibel, Y Ye, RK Hughes, W Bai, C Lau, H Shiwani, et al. "Precision measurement of cardiac structure and function in cardiovascular magnetic resonance using machine learning". In: *Journal of Cardiovascular Magnetic Resonance* 24.1 (2022), p. 16.

[60] P Vijayaraman, P Pokharel, FA Subzposh, JW Oren, RH Storm, SA Batul, DA Beer, G Hughes, G Leri, M Manganiello, et al. "His-Purkinje conduction system pacing optimized trial of cardiac resynchronization therapy vs biventricular pacing: HOT-CRT clinical trial". In: *Clinical Electrophysiology* 9.12 (2023), pp. 2628–2638.

[61] H Bader, S Garrigue, S Lafitte, S Reuter, P Jaïs, M Haïssaguerre, J Bonnet, J Clementy, and R Roudaut. "Intra-left ventricular electromechanical asynchrony: a new independent predictor of severe cardiac events in heart failure patients". In: *Journal of the American College of Cardiology* 43.2 (2004), pp. 248–256.

[62] M Sermesant, R Chabiniok, P Chinchapatnam, T Mansi, F Billet, P Moireau, JM Peyrat, K Wong, J Relan, K Rhode, et al. "Patient-specific electromechanical models of the heart for the prediction of pacing acute effects in CRT: a preliminary clinical validation". In: *Medical image analysis* 16.1 (2012), pp. 201–215.

[63] SG Duckett, M Ginks, AK Shetty, J Bostock, JS Gill, S Hamid, S Kapetanakis, E Cunliffe, R Razavi, G Carr-White, et al. "Invasive acute hemodynamic response to guide left ventricular lead implantation predicts chronic remodeling in patients undergoing cardiac resynchronization therapy". In: *Journal of the American College of Cardiology* 58.11 (2011), pp. 1128–1136.

[64] B Paun, B Bijnens, T Iles, PA Iaizzo, and C Butakoff. "Patient independent representation of the detailed cardiac ventricular anatomy". In: *Medical image analysis* 35 (2017), pp. 270–287.

[65] T Arts, P Bovendeerd, FW Prinzen, and RS Reneman. "Relation between left ventricular cavity pressure and volume and systolic fiber stress and strain in the wall". In: *Biophysical journal* 59.1 (1991), pp. 93–102.

[66] YC Fung. "Mathematical representation of the mechanical properties of the heart muscle". In: *Journal of biomechanics* 3.4 (1970), pp. 381–404.

[67] JC Kentish, H Ter Keurs, L Ricciardi, J Bucx, and M Noble. "Comparison between the sarcomere length-force relations of intact and skinned trabeculae from rat right ventricle. Influence of calcium concentrations on these relations." In: *Circulation research* 58.6 (1986), pp. 755–768.

A AHA regions

The LV free wall (LVfw) and the interventricular septum (IVS) were subdivided according to the 16-region AHA segmentation [47]. The LVfw comprises 11 segments (4 basal, 4 medial, and 3 apical), while the IVS comprises 5 segments (2 basal, 2 medial, and 1 apical). For the RV free wall (RVfw), three longitudinal bands (basal, medial, and apical) were defined, with 3 circumferential divisions (anterior, lateral, inferior) in the basal and medial bands and 2 in the apical band.

The regions were defined using the universal ventricular coordinates (UVC) introduced in [48], which provide a global positioning system for three-dimensional biventricular geometries through four scalar fields: apicobasal, transmural, rotational, and transventricular coordinates, each obtained as the solution of a Laplace problem. In this work, the transmural coordinate was not required.

Figure A.1 illustrates the three coordinates used to define the AHA regions on a patient-specific biventricular geometry, together with the corresponding bullseye representation. The transventricular coordinate (Fig. A.1A) distinguishes between the LV (blue cavity) and RV (purple cavity).

The apicobasal coordinate $\mathfrak{z}$ (Fig. A.1B), defined in $[0, 1]$, represents the normalized distance along the ventricular long axis from apex to base. To ensure a smooth and uniform variation of $\mathfrak{z}$, the geodesic normalization approach proposed in [64] was employed. Specifically, the shortest geodesic path from apex to base was computed, and the initial Laplace solution was reparameterized along this path as a function of normalized distance.

The basal, medial, and apical regions were defined by partitioning the interval $[0, 1]$ into three equal segments, corresponding to $\mathfrak{z} < \frac{1}{3}$, $\frac{1}{3} \leq \mathfrak{z} < \frac{2}{3}$, and $\mathfrak{z} \geq \frac{2}{3}$, respectively.

The rotational coordinate (Fig. A.1C), defined in $[-\pi, \pi]$, represents the circumferential position around the ventricular long axis. Circumferential sectors were obtained by partitioning this interval into sub-intervals corresponding to the desired number of regions and assigning nodes based on their rotational coordinate. The stars in the bullseye representation indicate the regions corresponding to the IVS.

The activation time for each region was defined as the mean electrical activation time over all nodes within that region. In the following, each region is referred to as a *patch*.

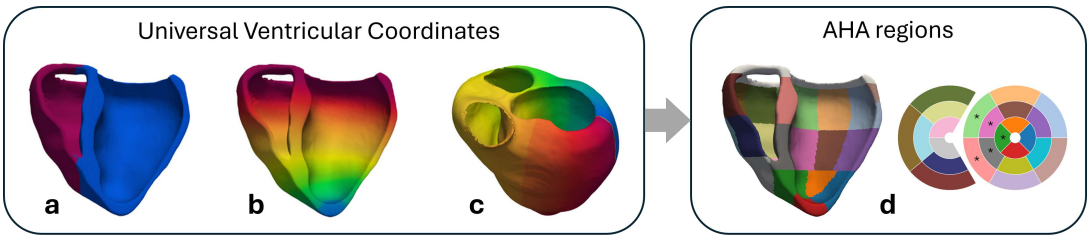

Figure A.1: UVC on a patient-specific biventricular geometry to define AHA regions. **a**: transventricular coordinate, **b**: apicobasal coordinate, **c**: rotational coordinate. **d**: AHA regions are represented in bullseye form, where the stars indicate the IVS.

B CircAdapt modules

In this appendix, we summarize the main governing equations of the CircAdapt model. Before introducing the MultiPatch formulation, we first describe the computation of wall tension in a uniform wall, as originally formulated in the TriSeg model [22], which represents the three ventricular walls enclosing two cavities.

B.1 The original CircAdapt model

The one-fiber model of [65] describes a pressurized cavity enclosed by a wall composed of fibers embedded in a soft incompressible material. Within the CircAdapt framework, this model is evaluated at the mid-wall level.

An actively contracting chamber $c \in \{\mathrm{LV}, \mathrm{RV}, \mathrm{LA}, \mathrm{RA}\}$ is described by the state variables cavity volume V_c, contractile element length of the sarcomere L_c^{cont}, and contractility C_c (B.21). Blood inflow and outflow induce changes in cavity volume V_c, which in turn determine cavity pressure.

In the original CircAdapt model [21], cavity pressures are derived from cavity volumes as follows. The cavity volume V_c determines the mid-wall area A_c^{mid}, defined as the surface dividing the wall volume in two equal parts along the radial direction. The mid-wall volume is given by

$$V_c^{\mathrm{mid}} = V_c + \frac{1}{2} V_c^{\mathrm{wall}}, \tag{B.1}$$

where V_c^{wall} denotes the wall volume.

Chambers are approximated as spheres, leading to the following relations between volume and surface:

$$C_c^{\mathrm{mid}} = \left(\frac{4\pi}{3V_c^{\mathrm{mid}}} \right)^{1/3}, \tag{B.2}$$

$$A_c^{\mathrm{mid,tot}} = \frac{4\pi}{\left(C_c^{\mathrm{mid}}\right)^2}, \tag{B.3}$$

$$A_c^{\mathrm{mid}} = A_c^{\mathrm{mid,tot}} - A_c^{\mathrm{mid,dead}}, \tag{B.4}$$

where C_c^{mid} is the mid-wall curvature (inverse radius), and $A_c^{\mathrm{mid,dead}}$ represents the non-contractile area (e.g., valve orifices).

The mid-wall area determines the myofiber strain. The natural fiber strain E_c^{fib} is computed as

$$E_c^{\mathrm{fib}} = \frac{1}{2} \ln \left(\frac{A_c^{\mathrm{mid}}}{A_c^{\mathrm{mid,ref}}} \right), \tag{B.5}$$

where $A_c^{\mathrm{mid,ref}}$ is the reference mid-wall area, computed from (B.4) using reference values of the volumes.

Given the fiber strain, a constitutive model is used to compute the corresponding myofiber stress σ_c^{fib}. This stress drives the wall tension. In CircAdapt, the relation between mid-wall tension T_c^{mid}, mid-wall area A_c^{mid}, and fiber stress is derived from conservation of energy:

$$T_c^{\mathrm{mid}} \, \mathrm{d}A_c^{\mathrm{mid}} = \sigma_c^{\mathrm{fib}} V_c^{\mathrm{wall}} \, \mathrm{d}E_c^{\mathrm{fib}}. \tag{B.6}$$

Using (B.5), this yields

$$T_c^{\mathrm{mid}} = \frac{\sigma_c^{\mathrm{fib}} V_c^{\mathrm{wall}}}{2A_c^{\mathrm{mid}}}. \tag{B.7}$$

In the TriSeg model [22], the geometries of the three ventricular walls are iteratively adjusted to satisfy mechanical equilibrium at their junction. As a result, wall areas A_c^{mid} and curvatures C_c^{mid} evolve during the iteration. Once wall tension and curvature are known, the transmural pressure is computed via Laplace's law:

$$p_c^{\mathrm{trans}} = 2T_c^{\mathrm{mid}} C_c^{\mathrm{mid}}. \tag{B.8}$$

Cavity pressure is then obtained by adding the pericardial pressure:

$$p_c = p_c^{\mathrm{trans}} + p_{\mathrm{peri}}.$$

Cavity pressures are subsequently used to update flows across valves and, consequently, cavity volumes.

To account for intraventricular and transventricular heterogeneity in activation and deformation, we adopt the MultiPatch approach [27].

B.2 The MultiPatch model

Let us consider a wall subdivided into n patches. To simplify notation, cavity-related variables are denoted without subscripts (e.g., V for cavity volume), whereas quantities indexed by j refer to the j-th patch. In particular, V_j and A_j^{ref} denote the patch volume and reference area, respectively. The superscript "mid" is omitted for brevity.

In this formulation, stress and strain are allowed to vary across patches, and therefore Eq. (B.7) no longer holds uniformly over the wall. To solve the resulting equilibrium problem, the wall tension T is linearized around a reference configuration corresponding to the wall area at zero tension, denoted by A_0:

$$T(A) \approx \frac{\mathrm{d}T}{\mathrm{d}A}(A - A_0). \tag{B.9}$$

For each patch, an analogous linearized relation is introduced:

$$T_j(A_j) \approx \frac{\mathrm{d}T_j}{\mathrm{d}A_j}(A_j - A_{0,j}), \tag{B.10}$$

where $A_{0,j}$ is the zero-tension area of patch j.

Since transmural pressure and curvature are common to all patches within a wall, Laplace's law implies that the wall tension is uniform, i.e., $T_j = T$ for all patches. When the wall tension vanishes, the total mid-wall area equals the sum of the zero-tension areas of all patches:

$$A_0 = \sum_{j=1}^{n} A_{0,j}. \tag{B.11}$$

Differentiating Eq. (B.11) with respect to T and inverting yields:

$$\frac{\mathrm{d}T}{\mathrm{d}A} = \frac{1}{\sum_{j=1}^{n} \left(\frac{\mathrm{d}T_j}{\mathrm{d}A_j}\right)^{-1}}, \tag{B.12}$$

which defines the effective wall stiffness.

Equations (B.11) and (B.12) are then used in Eq. (B.9) to determine the wall tension T for a given wall area A within the TriSeg iterative scheme. Once the TriSeg solution is obtained, the transmural pressure p_c^{trans} is computed using Laplace's law (B.8).

Given the wall tension, the patch areas A_j are recovered from Eq. (B.10). The fiber strain E_j^{fib} is then computed for each patch using the patch-wise equivalent of Eq. (B.5), and the corresponding fiber stress σ_j^{fib} is obtained from the sarcomere model (Appendix B.3). Different activation times are assigned to each patch, resulting in heterogeneous stress and strain distributions.

To evaluate Eqs. (B.11) and (B.12), the zero-tension areas $A_{0,j}$ and patch stiffnesses $\frac{\mathrm{d}T_j}{\mathrm{d}A_j}$ must be computed. Assuming spherical geometry and isotropic deformation, the patch area satisfies:

$$A_j = \left(\frac{L_j^{\mathrm{s}}}{L_j^{\mathrm{s,ref}}}\right) A_j^{\mathrm{ref}}, \tag{B.13}$$

where L_j^{s} is the sarcomere length and $L_j^{\mathrm{s,ref}}$ its reference value.

Since L_j^{s} is not directly available during the TriSeg iteration, an initial estimate is obtained using the contractile element length L_j^{cont} (see Appendix B.3), yielding:

$$E_{j,i}^{\mathrm{fib}} = \ln\left(\frac{L_j^{\mathrm{cont}}}{L_j^{\mathrm{s,ref}}}\right). \tag{B.14}$$

From this estimate, the sarcomere model provides the corresponding fiber stress $\sigma_{j,i}^{\mathrm{fib}}$ and stiffness $\frac{\mathrm{d}\sigma_{j,i}^{\mathrm{fib}}}{\mathrm{d}E_{j,i}^{\mathrm{fib}}}$. The induced patch tension is then given by

$$T_{j,i} = \frac{\sigma_{j,i}^{\mathrm{fib}} V_j}{2A_{j,i}}, \tag{B.15}$$

where $A_{j,i}$ is the estimated patch area.

The patch stiffness follows as

$$\frac{\mathrm{d}T_{j,i}}{\mathrm{d}A_{j,i}} = \left(\frac{\mathrm{d}\sigma_{j,i}^{\mathrm{fib}}}{\mathrm{d}E_{j,i}^{\mathrm{fib}}} - 2\sigma_{j,i}^{\mathrm{fib}}\right) \frac{V_j}{4A_{j,i}^2}. \tag{B.16}$$

Finally, the zero-tension area is obtained from Eq. (B.10):

$$A_{0,j} = A_{j,i} - \frac{T_{j,i}}{\mathrm{d}T_{j,i}/\mathrm{d}A_{j,i}}. \tag{B.17}$$

B.3 Sarcomere mechanics

In this section, we describe the sarcomere module of CircAdapt as introduced in the original model [21], where the subscript c denotes the cavity. In the MultiPatch formulation, the cardiac wall is subdivided into N patches, so that each variable indexed by c gives rise to N patch-specific equations, allowing mechanical parameters to vary across patches.

A sarcomere is modeled using a three-element Hill-type contraction model [66]. The contractile element, with length L_c^{cont}, is arranged in series with an elastic element of length L_c^{elast}, and this series combination is in parallel with an additional elastic element. The total sarcomere length is given by

$$L_c^{\mathrm{s}} = L_c^{\mathrm{elast}} + L_c^{\mathrm{cont}} = L_c^{\mathrm{s,ref}} \exp\left(E_c^{\mathrm{fib}}\right), \tag{B.18}$$

where $L_c^{\mathrm{s,ref}}$ is the reference sarcomere length corresponding to the reference wall area, and E_c^{fib} is the natural myofiber strain, defined as

$$E_c^{\mathrm{fib}} = \ln\left(\frac{L_c^{\mathrm{s}}}{L_c^{\mathrm{s,ref}}}\right). \tag{B.19}$$

Sarcomere active stress The contractile element length L_c^{cont} evolves over time according to

$$\dot{L}_c^{\mathrm{cont}} = \frac{\mathrm{d}L_c^{\mathrm{cont}}}{\mathrm{d}t} = v^{\max}\left[\frac{L_c^{\mathrm{s}} - L_c^{\mathrm{cont}}}{L^{\mathrm{elast,iso}}} - 1\right], \tag{B.20}$$

where $L^{\mathrm{elast,iso}}$ is the length of the series elastic element during isovolumetric contraction, and $v^{\max}$ is the maximum contraction velocity.

Active stress also depends on time through the contractility variable C_c, a phenomenological quantity representing the density of cross-bridges within the sarcomere. Contractility increases upon activation and exhibits a rise and decay phase with distinct time constants. The rate of increase depends on sarcomere length [67]. Active stress increases with contractility, contractile element length, and series elastic element stretch.

The evolution of contractility is modeled as

$$\dot{C}_c = f_c^{\mathrm{rise}}(t) C_c^{\mathrm{s}}\left(L_c^{\mathrm{cont}}\right) - f_c^{\mathrm{decay}}(t) C_c. \tag{B.21}$$

The rise function f_c^{rise} describes the formation of cross-bridges:

$$f_c^{\mathrm{rise}}(t) = \frac{1}{t_c^{\mathrm{rise}}} 0.02\, x_c^3 (8 - x_c)^2 \exp(-x_c), \tag{B.22}$$

$$x_c(t) = \min\left(8, \max\left(0, \frac{t - t_c^{\mathrm{act}}}{t_c^{\mathrm{rise}}}\right)\right), \tag{B.23}$$

where t_c^{act} is the activation onset time and

$$t_c^{\mathrm{rise}} = 0.55\, \tau^{\mathrm{R}}\, t_c^{\mathrm{act,ref}}.$$

The activation time t_c^{act} is defined relative to the beginning of the cardiac cycle t^{bt}:

$$t^{\mathrm{bt}} = n\, t_{\mathrm{cycle}}, \tag{B.24}$$

such that

$$t_c^{\mathrm{act}} = t^{\mathrm{bt}} \tag{B.25}$$

for the atria, and

$$t_c^{\mathrm{act}} = t^{\mathrm{bt}} + t^{\mathrm{AV}} + \Delta t_{\mathrm{c}}^{\mathrm{act}} \tag{B.26}$$

for the ventricles, where $\Delta t_{\mathrm{c}}^{\mathrm{act}}$ is the patch-wise activation delay from the EP model and t^{AV} is the atrioventricular delay.

The decay of contractility is governed by

$$f_c^{\mathrm{decay}}(t) = \frac{1}{2t_c^{\mathrm{decay}}}\left[1 + \sin\left(\mathrm{sign}(y_c)\min\left(\frac{\pi}{2}, |y_c|\right)\right)\right],$$

$$y_c(t) = \frac{t - t_c^{\mathrm{act}} - t_c^{\mathrm{act,dur}}}{t_c^{\mathrm{decay}}},$$

with

$$t_c^{\text{decay}} = 0.33\,\tau^{\text{D}}\,t_c^{\text{act,ref}},$$

and contraction duration

$$t_c^{\text{act,dur}} = (0.65 + 1.0570\,L_c^{\text{norm}})\,t_c^{\text{act,ref}}.$$

Here, the normalized sarcomere length is defined as

$$L_c^{\text{norm}} = \max\left(0.0001, \frac{L_c^{\text{cont}}}{L^{\text{act0,ref}}} - 1\right),$$

where $L^{\text{act0,ref}}$ is the sarcomere length at zero active stress.

The function C_c^{s} accounts for the dependence of cross-bridge formation on sarcomere length:

$$C_c^{\text{s}}\left(L_c^{\text{cont}}\right) = \tanh\left(0.75 \cdot 9.1204\,(L_c^{\text{norm}})^2\right).$$

Finally, the active fiber stress is given by

$$\sigma_c^{\text{fib,act}} = L^{\text{act0,ref}}\,\sigma^{\text{act,max}}\,C_c\,L_c^{\text{norm}}\,\frac{L_c^{\text{s}} - L_c^{\text{cont}}}{L^{\text{elast,iso}}}, \tag{B.27}$$

where $\sigma^{\text{act,max}}$ is the maximum isometric active stress.

Sarcomere passive stress The passive stress $\sigma_c^{\text{fib,pas}}$ is modeled as the sum of two contributions,

$$\sigma_c^{\text{fib,pas}} = \sigma_c^{\text{fib,tit}} + \sigma_c^{\text{fib,ecm}}, \tag{B.28}$$

representing the stresses generated by intracellular structures (primarily titin, a key structural protein of the sarcomere anchored to the Z-disc) and by the extracellular matrix (ECM), respectively.

Both components depend on the passive fiber stretch, defined as

$$\lambda_c^{\text{pas}} = \frac{L_c^{\text{s}}}{L^{\text{pas0,ref}}},$$

where $L^{\text{pas0,ref}}$ is the sarcomere length at zero passive stress and L_c^{s} is the total sarcomere length.

The titin contribution is modeled as

$$\sigma_c^{\text{fib,tit}} = 0.01\,\sigma^{\text{act,max}}\left(\lambda_c^{\text{pas}\,k^{\text{tit}}} - 1\right),$$

where $\sigma^{\text{act,max}}$ is the maximal isometric stress, and the exponent k^{tit} is defined as

$$k^{\text{tit}} = 2\frac{L^{\text{s,ref}}}{L^{\text{s,pas}}},$$

where $L^{\text{s,pas}}$ is a characteristic length scale governing passive stiffness.

The ECM contribution is modeled as a stiffer nonlinear response:

$$\sigma_c^{\text{fib,ecm}} = 0.0349\,\sigma^{\text{pas,max}}\left(\lambda_c^{\text{pas}\,10} - 1\right), \tag{B.29}$$

where $\sigma^{\text{pas,max}}$ is an empirical parameter.

Sarcomere total stress The total myofiber stress σ_c^{fib} is given by the sum of the active stress (B.27) and the passive stress (B.28):

$$\sigma_c^{\text{fib}} = \sigma_c^{\text{fib,act}} + \sigma_c^{\text{fib,pas}}. \tag{B.30}$$

The sarcomere stiffness κ_c^{fib} is defined as the derivative of total fiber stress with respect to fiber strain:

$$\kappa_c^{\text{fib}} = \frac{\partial\sigma_c^{\text{fib}}}{\partial E_c^{\text{fib}}} = \frac{\partial\sigma_c^{\text{fib,act}}}{\partial E_c^{\text{fib}}} + \frac{\partial\sigma_c^{\text{fib,pas}}}{\partial E_c^{\text{fib}}}, \tag{B.31}$$

where

$$\frac{\partial\sigma_c^{\text{fib,act}}}{\partial E_c^{\text{fib}}} = L^{\text{act0,ref}}\,\sigma^{\text{act,max}}\,C_c\,L_c^{\text{norm}}\,\frac{L_c^{\text{s}}}{L^{\text{elast,iso}}},$$

$$\frac{\partial\sigma_c^{\text{fib,pas}}}{\partial E_c^{\text{fib}}} = 0.01\,k^{\text{tit}}\,\sigma^{\text{act,max}}\lambda_c^{\text{pas}\,k^{\text{tit}}} + 0.0349 \cdot 10\,\sigma^{\text{pas,max}}\lambda_c^{\text{pas}\,10}.$$

B.4 Vessel module

The tube module represents compliant blood vessels capable of propagating pressure–flow waves superimposed on a mean flow [21]. Vessels directly connected to the heart, namely the aorta (AO), pulmonary artery (AP), venae cavae (VC), and pulmonary veins (VP), are modeled using this formulation.

The lumen cross-sectional area is computed as

$$A_t = \frac{V_t}{l_t}, \tag{B.32}$$

where V_t is the vessel volume and l_t is the segment length.

Using a fibrous tube model [65], the average fiber stretch λ_t is given by

$$\lambda_t = \left(1 + \frac{2V_t}{V_t^{\text{wall}}}\right)^{1/3} = \left(1 + \frac{2A_t}{A_t^{\text{wall}}}\right)^{1/3}, \tag{B.33}$$

where A_t^{wall} is the wall cross-sectional area and $V_t^{\text{wall}} = A_t^{\text{wall}} l_t$ is the wall volume.

The vessel pressure depends on the stretch λ_t as

$$p_t = \sigma_t(\lambda_t)\, \lambda_t^{-3}, \tag{B.34}$$

where σ_t is the mean Cauchy fiber stress, modeled by the constitutive law

$$\sigma_t(\lambda_t) = \sigma_t^{\text{ref}} \left(\frac{\lambda_t}{\lambda_t^{\text{ref}}}\right)^{k_t}. \tag{B.35}$$

Here, k_t is a stiffness exponent, λ_t^{ref} is the reference fiber stretch,

$$\lambda_t^{\text{ref}} = \left(1 + \frac{2V_t^{\text{ref}}}{V_t^{\text{wall}}}\right)^{1/3},$$

and σ_t^{ref} is the corresponding reference stress,

$$\sigma_t^{\text{ref}} = p_t^{\text{ref}} \left(\lambda_t^{\text{ref}}\right)^3,$$

with p_t^{ref} denoting the reference pressure.

Combining the above relations yields the current vessel pressure:

$$p_t = p_t^{\text{ref}} \left(\frac{A_t^{\text{wall}} + 2A_t}{A_t^{\text{wall}} + 2A_t^{\text{ref}}}\right)^{\frac{k_t - 3}{3}}, \tag{B.36}$$

where A_t^{ref} is the reference cross-sectional area and $V_t^{\text{ref}} = A_t^{\text{ref}} l_t$ is the reference vessel volume.

B.5 Periphery

The pulmonary (pulm) and systemic (sys) periphery are modeled as resistive elements. The current pressure drop Δp_{py}, for $py \in \{\text{pulm}, \text{sys}\}$, is defined as the difference between the pressure in the inflow artery p_t^{prox} and that in the outflow vein p_t^{dist}:

$$\Delta p_{py} = p_t^{\text{prox}} - p_t^{\text{dist}}. \tag{B.37}$$

The corresponding resistances are computed as

$$R_{py} = \frac{\Delta p_{py}^{\text{ref}}}{q^{\text{rest}}}, \tag{B.38}$$

where $\Delta p_{py}^{\text{ref}}$ is the reference arteriovenous pressure drop and q^{rest} is the mean systemic flow at rest.

The resulting flow through the peripheral circulation is then given by

$$q_{py} = \frac{\Delta p_{py}}{R_{py}}. \tag{B.39}$$

C CircAdapt Global Sensitivity Analysis

A global sensitivity analysis (GSA) was performed on the CircAdapt model to identify the input parameters that most strongly influence the six target output volumes. The set of model parameters considered in the analysis is reported in Table 6.

After fixing patient-specific inputs (highlighted in gray in Table 6), the GSA was conducted separately for each patient. The resulting total Sobol indices are shown in Figure C.1. Each parameter was varied within predefined physiological ranges around its baseline value (see Table 6), consistent with values reported in [27].

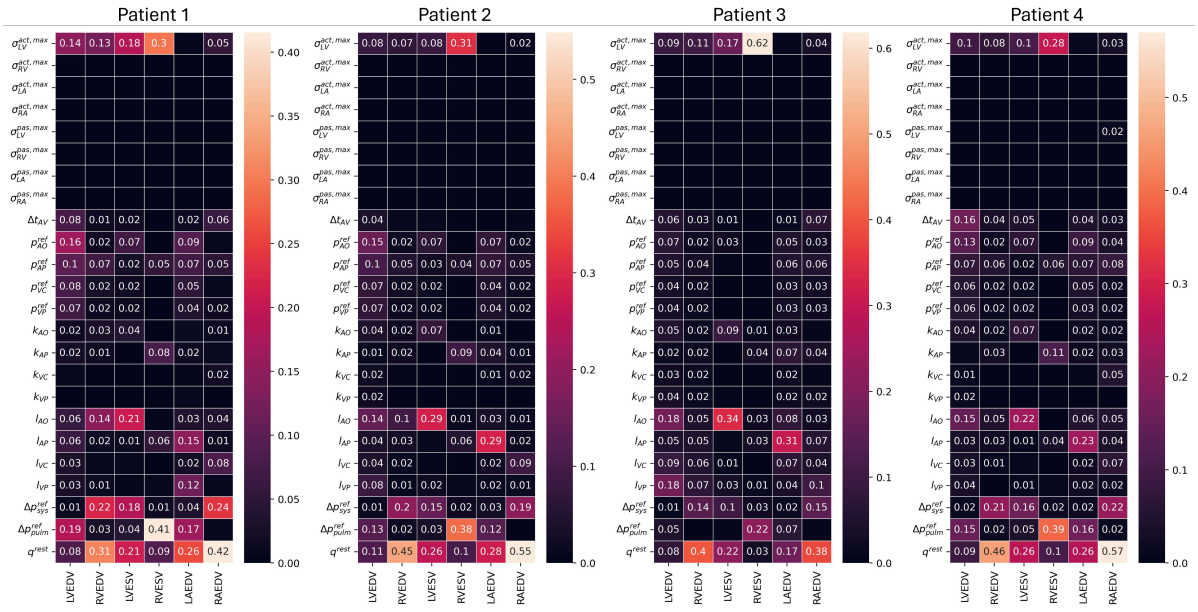

Figure C.1: Heatmap of total Sobol indices obtained from the global sensitivity analysis for the four patients.